Chapter 4
2D–3D Phononic Crystals

A. Sukhovich, J.H. Page, J.O. Vasseur, J.F. Robillard, N. Swinteck, and Pierre A. Deymier

Abstract This chapter presents a comprehensive description of the properties of phononic crystals ranging from spectral properties (e.g., band gaps) to wave vector properties (refraction) and phase properties. These properties are characterized by experiments and numerical simulations.

4.1 Introduction

In this chapter, we focus on 2D and 3D phononic crystals, which, thanks to their spatial periodicity, allow the observation of new unusual phenomena as compared to the 1D crystals discussed in the previous chapter. In experimental studies, 2D crystals usually employ rods as scattering units, while 3D crystals are realized as arrangements of spheres. It is common in theoretical studies of phononic crystals to investigate crystals with scattering units that are simply air voids (e.g., empty cylinders) in a matrix. Although there are many different ways of realizing the

A. Sukhovich (✉)
Laboratoire Domaines Océaniques, UMR CNRS 6538, UFR Sciences et Techniques, Université de Bretagne Occidentale, Brest, France
e-mail: sukhovich@univ-brest.fr

J.H. Page
Department of Physics and Astronomy, University of Manitoba, Winnipeg, MB, Canada R3T 2N2
e-mail: jhpage@cc.umanitoba.ca

J.O. Vasseur • J.F. Robillard
Institut d'Electronique, de Micro-électronique et de Nanotechnologie, UMR CNRS 8520, Cité Scientifique 59652, Villeneuve d'Ascq Cedex, France
e-mail: Jerome.Vasseur@univ-lille1.fr; jean-francois.robillard@isen.fr

N. Swinteck • P.A. Deymier
Department of Materials Science and Engineering, University of Arizona, Tucson, AZ 85721, USA
e-mail: swinteck@email.arizona.edu; deymier@email.arizona.edu

P.A. Deymier (ed.), *Acoustic Metamaterials and Phononic Crystals*, Springer Series in Solid-State Sciences 173, DOI 10.1007/978-3-642-31232-8_4,

phononic crystal theoretically and experimentally (by varying material of the scattering units and the host matrix), one condition is always observed: the characteristic size of a scattering unit (rod or sphere) and a lattice constant should be on the order of the wavelength of the incident radiation to ensure that the particular crystal features arising from its regularity affect the wave propagating through the crystal. In other words, the frequency range of the crystal operation is set by the characteristic dimensions of the crystal (i.e., the size of its unit scatterer and its lattice constant). The exception from this rule, however, is resonant sonic materials, which exhibit a profound effect on the propagating radiation, whose wavelength can be as much as two orders of magnitude larger than the characteristic size of the structure, as was shown by Liu et al. [1, 2].

As described in Chap. 10, the regularity of the arrangement of scattering units of the phononic crystal gives rise to Bragg reflections of the acoustic or elastic waves that are multiply scattered inside the crystal. Their constructive or destructive interference creates ranges of frequencies at which waves are either allowed to propagate (pass bands) or blocked in one (stop bands) or any direction (complete band gaps). The width of the band gap obviously depends on the crystal structure and increases with the increase of density contrast between the material of the scattering unit and that of a host matrix. Switching from a liquid matrix to the solid one, e.g., from water to epoxy, which can support both longitudinal and transverse polarizations, results in even larger band gaps, as was shown by Page et al. [3].

As an example of a 2D phononic crystal, consider a crystal made of cylinders assembled in a *triangular* Bravais lattice, whose points are located at the vertices of the equilateral triangles. Figure 4.1 presents the diagram of the direct and reciprocal lattices with corresponding primitive vectors $\vec{a}_1, \vec{a}_2$ and $\vec{b}_1, \vec{b}_2$. Since $|\vec{a}_1| = |\vec{a}_2| = a$, where a is a lattice constant, it follows from the usual definition of reciprocal lattice vectors $\vec{a}_i \cdot \vec{b}_j = 2\pi\delta_{ij}$, where δ_{ij} is the Kronecker delta symbol, that $\left|\vec{b}_1\right| = \left|\vec{b}_2\right| = 4\pi/\sqrt{3}a$. By working out components of $\vec{b}_1$ and $\vec{b}_2$, one can be convinced that the reciprocal lattice of a triangular lattice is also a triangular lattice but rotated through 30° with respect to a direct lattice. Both direct and reciprocal lattices possess six-fold symmetry. The first Brillouin zone has a shape of a hexagon with two main symmetry directions, which are commonly referred to as ΓM and ΓK (Fig. 4.1).

As an example of a 3D crystal, let us consider a collection of spheres assembled in a face-centered cubic (FCC) structure, which is obtained from the simple-cubic lattice by adding one sphere to the center of every face of the cubic unit cell. Because of its high degree of symmetry, phononic crystals with this structure have been extensively investigated, both theoretically and experimentally. Figure 4.2 shows the direct lattice of the FCC structure along with the corresponding reciprocal lattice, which turns out to be a body-centered cubic (BCC) crystal structure (obtained from the simple-cubic structure by adding one atom in the center of its unit cell). Also displayed are the sets of primitive vectors $\vec{a}_1, \vec{a}_2, \vec{a}_3$ and $\vec{b}_1, \vec{b}_2, \vec{b}_3$ of both lattices. It can be easily seen from Fig. 4.2 that with this particular choice of the primitive vectors of the direct lattice we have $|\vec{a}_1| = |\vec{a}_2| = |\vec{a}_3| = a/\sqrt{2}$, and

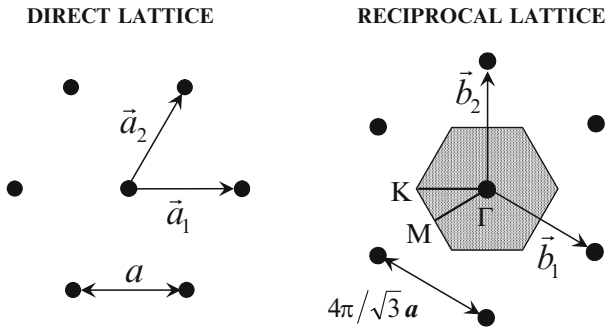

Fig. 4.1 The direct and reciprocal lattices of the 2D phononic crystals, which were investigated experimentally. The *shaded hexagon* indicates the first Brillouin zone. In the actual phononic crystal the rods were positioned at the points of the direct lattice (perpendicular to the plane of the figure)

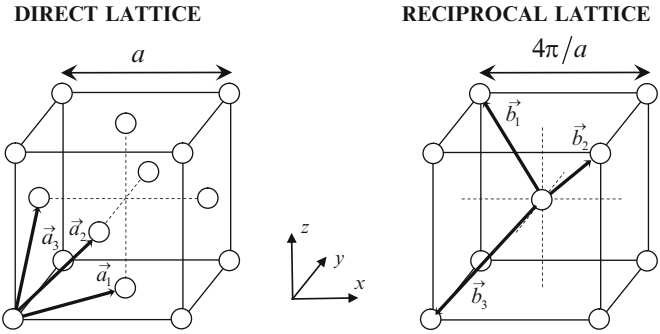

Fig. 4.2 The direct (FCC) and reciprocal (BCC) crystal lattices of the 3D phononic crystals

$\left|\vec{b}_1\right| = \left|\vec{b}_2\right| = \left|\vec{b}_3\right| = 2\sqrt{3}\pi/a$, where a is the length of the cube edge in the direct lattice.

The first Brillouin zone of the FCC lattice is a truncated octahedron and coincides with the Wigner-Seitz cell of the BCC lattice. It is presented in Fig. 4.3 along with its high symmetry directions. With respect to the coordinate system in Fig. 4.2, the coordinates of the high symmetry points (in units of $2\pi/a$) are: Γ [000], X [100], L [½ ; ½ ; ½], W [½ ; 1; 0], and K [¾; ¾; 0]. The investigation of the figure reveals that direction ΓL coincides with the direction also known as the [111] direction, i.e., a direction along the body diagonal of the conventional FCC unit cell, shown in Fig. 4.2.

A simple way of realizing a 3D crystal with the FCC Bravais lattice is by stacking the crystal layers along the [111] direction. The touching spheres are close packed in an ABCABC. . . sequence, which is shown in Fig. 4.4. The spheres

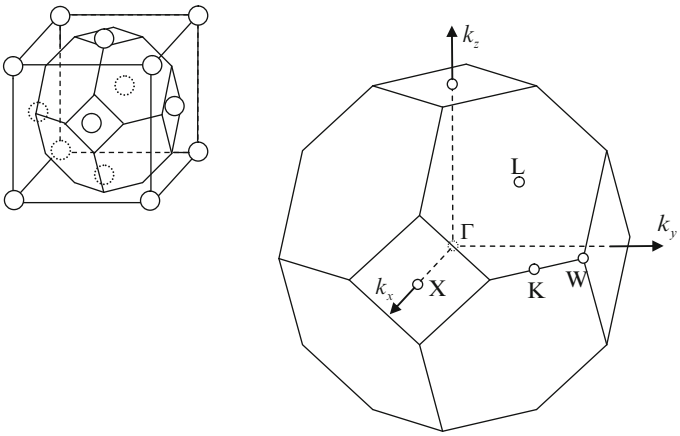

Fig. 4.3 The first Brillouin zone of the FCC lattice and its high symmetry points

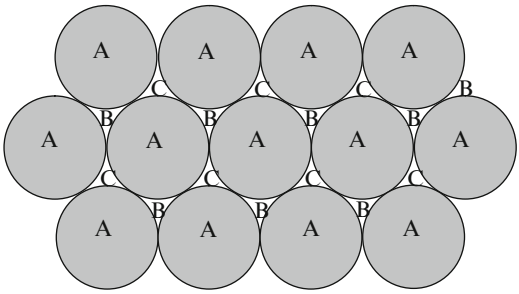

Fig. 4.4 Schematic diagram explaining the formation of a 3D crystal in a ABCABC. . . sequence

belonging to the first layer are denoted by the letter A. The next layer is formed by placing the spheres in the interstitials indicated by the letter B, and the third layer is formed by placing spheres in the interstitials of the second layer, which are denoted by the letter C. The sequence is then repeated again with the fourth layer beads to occupy interstitials in the third layer, which are positioned directly above beads denoted by the letter A. This packing results in the highest filling ratio of 74 %.

In this chapter, the dramatic effects of lattice periodicity on wave transport in 2D and 3D phononic crystals will be illustrated using these two representative crystal structures. Section 4.2 summarizes how such effects can be investigated experimentally, with emphasis on measurement techniques in the ultrasonic frequency range. Section 4.3 discusses the various mechanisms that can lead to the formation of band gaps, a topic that has been of central interest since the first calculations and experimental observations in phononic crystals. The rest of the chapter is concerned with phenomena that occur in the pass bands, starting with negative refraction in Sect. 4.4, the achievement of super-resolution lenses in Sect. 4.5 and band structure design and its impact on refraction in Sect. 4.6.

4.2 Experiments: Crystal Fabrication and Experimental Methods

4.2.1 Sample Preparation

4.2.1.1 2D Phononic Crystals

In this section we will consider the practical aspects of phononic crystal fabrication for the examples of 2D and 3D phononic crystals used by Sukhovich et al. [4, 5] and Yang et al. [6, 7] during their experiments on wave transport, negative refraction and focusing of ultrasound waves (see Sects. 4.3 and 4.4.). The 2D crystals were made of stainless steel rods assembled in a triangular crystal lattice and immersed in a liquid matrix. To ensure that the operational frequency of the crystals was in the MHz range, the characteristic dimensions of the crystals, lattice constant and rod diameter (1.27 mm and 1.02 mm correspondingly), were chosen to be comparable to the wavelength of ultrasound in water at this frequency range (Fig. 4.5).

For reasons that will be explained in more detail later, the crystals were made in two different shapes. A rectangular-shaped crystal had 6 layers stacked along the ΓM direction (Fig. 4.6a). A prism-shaped crystal was also made; it had 58 layers, whose length was diminishing progressively to produce sides forming angles of 30°, 60° and 90°. In this geometry, the shortest and longest sides are perpendicular to the ΓM directions (Fig. 4.6b), and the third intermediate-length side is perpendicular to the ΓK direction.

The filling fraction was 58.4 %. The particular details of crystal design depended on the type of liquid, which filled the space between the rods. For the crystals immersed in and filled with water, the rods were kept in place by two parallel polycarbonate plates in which the required number of holes was drilled; the crystal could then be easily assembled by sliding the rod's into the holes in these top and bottom templates (Fig. 4.7a, b). The rectangular crystal was 14 cm high while the prism-shaped crystal height was 9 cm.

Since key properties of the phononic crystals follow from their periodicity, the quality of the samples is critically dependent on the accuracy with which their geometry is set. For example, special care must be taken to use as straight rods as possible. At the same time, the holes defining the rods' positions should be precisely drilled, preferably using an automated programmable drilling machine.

Another rectangular-shaped crystal (with all parameters identical to those of the first crystal) was constructed to enable the liquid surrounding the rods (methanol) to be different to the medium outside the crystal (water), and consequently its design was more complicated. First of all, all plastic parts were made of an alcohol-resistant plastic (PVC). The crystal was encapsulated in a cell, whose face walls were made of a very thin (0.01-mm) plastic film tightly wrapped around the crystal (plastic film produced commercially and available as a food wrap worked very

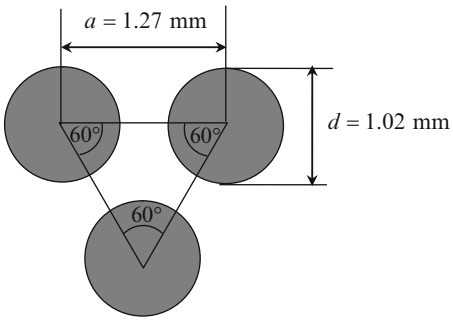

Fig. 4.5 Unit cell of a 2D phononic crystal

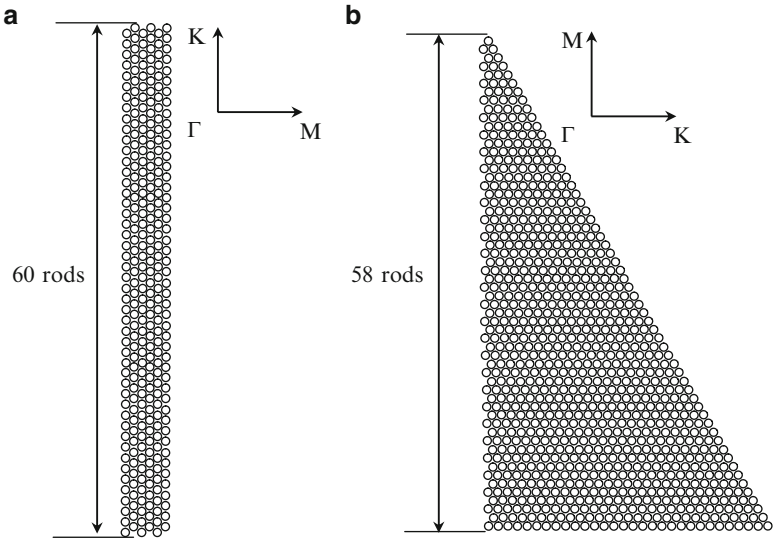

Fig. 4.6 Geometry of the 2D crystals. (**a**) Rectangular crystal. (**b**) Prism-shaped crystal

well). Finally, the edges of the cell were sealed from the surrounding water by two rubber O-rings. The design of the crystal is shown in Fig. 4.8.

The choice of the phononic crystal materials provided high density and velocity contrast, thus ensuring that most of the sound energy was scattered by the rods and concentrated in the host matrix. Table 4.1 provides values of the densities and sound velocities for the constituent materials of the 2D crystals.

4.2.1.2 3D Phononic Crystals

3D phononic crystals, used in the experiments by Yang et al. [6, 7] and by Sukhovich et al. [8, 9], were made out of very monodisperse tungsten carbide

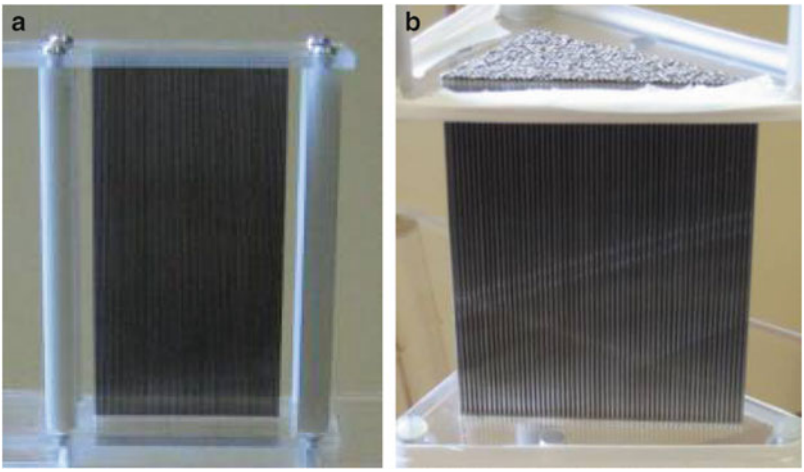

Fig. 4.7 2D crystals filled with and immersed in water: (**a**) rectangular crystal, (**b**) prism-shaped crystal

beads, 0.800 ± 0.0006 mm in diameter, immersed in reverse osmosis water. The beads were manually assembled in the FCC structure, with layers stacked along the cube body diagonal (the [111] direction) in an ABCABC... sequence. To ensure the absence of air bubbles trapped between the beads, the whole process of assembling crystals was conducted in water. To support the beads in the required structure, acrylic templates were used. The template consisted of a thick substrate with plastic walls attached to it (Fig. 4.9).

One can show that in order to keep beads in the FCC crystal lattice two kinds of walls should be used with sides inclined at angles $\alpha = 54.74^\circ$ and $\beta = 70.33^\circ$ above the horizontal, and with inner side lengths L_A and L_B. The values of L_A and L_B depend on the number of beads n along each side of the first crystal layer and the bead diameter d. These lengths are given by the following expressions:

$$L_A = (n - 1 + \tan\frac{\alpha}{2})d$$
$$L_B = (n - 1 + \tan\frac{\beta}{2}\cot 75^\circ)d \tag{4.1}$$

With 49 beads on each side of the bottom layer, (4.1) gives $L_A = 38.814$ mm and $L_B = 38.552$ mm.

In the experiments on the resonant tunneling of ultrasound pulses, the samples consisted of *two* 3D phononic crystals with the same number of layers and separated by an aluminum spacer of constant thickness. For brevity, these samples will be referred to as *double* 3D crystals. After the lower crystal was assembled, the spacer was placed on the top without disturbing beads of the crystal. The upper crystal was then assembled on the surface of the spacer. Spacer edges were machined at angles

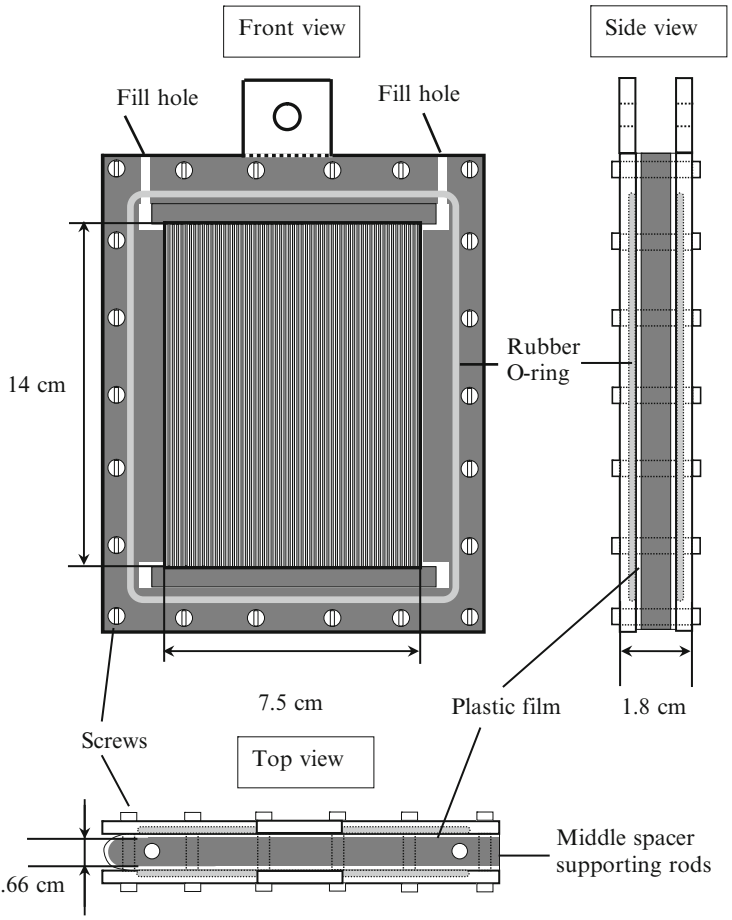

Fig. 4.8 Methanol-filled 2D crystal cell design

Table 4.1 Comparison of the physical properties of the constituent materials used for 2D phononic crystals [49]

Material	Density (g/cm^3)	Longitudinal velocity (mm/μs)	Shear velocity (mm/μs)
Stainless steel	7.89	5.80	3.10
Water	1.00	1.49	–
Methanol	0.79	1.10	–

matching the angles of the walls of the template. Also, the thickness of the spacer was calculated such that it replaced precisely an integer number of layers of the single crystal. This ensured that the beads resting on the spacer filled the entire available surface without leaving any gaps, enabling high-quality crystals to be

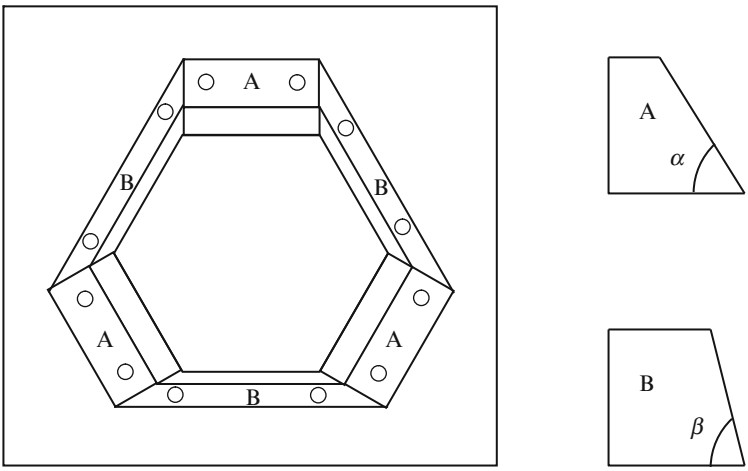

Fig. 4.9 Template for 3D phononic crystal (top view) with side views of walls A and B. Note that $\tan\alpha = \sqrt{2}$ and $\tan\beta = 2\sqrt{2}$

constructed. In most of the experiments, the thickness of the spacer was chosen to be 7.05 ± 0.01 mm.

The base of the template was made fairly thick (84.45 mm) to allow temporal separation between the ultrasonic pulses that was directly transmitted through the crystal, and all of its subsequent multiple reflections inside the substrate. The density and velocity mismatch in the case of 3D crystals was even larger than for 2D crystals, as tungsten carbide has density of 13.8 g/cm^3, longitudinal velocity of 6.6 mm/μs and shear velocity of 3.2 mm/μs. The actual sample (single 3D crystal) is shown in Fig. 4.10, while the close-up of its surface is presented in Fig. 4.11.

4.2.2 Experimental Methods

In the sonic and ultrasonic frequency ranges, the properties of phononic crystals are best studied experimentally by directing an incident acoustic or elastic wave towards the sample and measuring the characteristics of the outgoing wave, which was modified while propagating through the crystal. In practice, pulses are preferred to continuous monochromatic waves since pulses are much more convenient to work with. Due to their finite bandwidth, in a single experiment they allow information to be obtained over a wide frequency range. The use of pulses also facilitates the elimination of stray sound from the environment surrounding the crystal. In what follows, we describe two types of experiments, each used to investigate different aspects of phononic crystals.

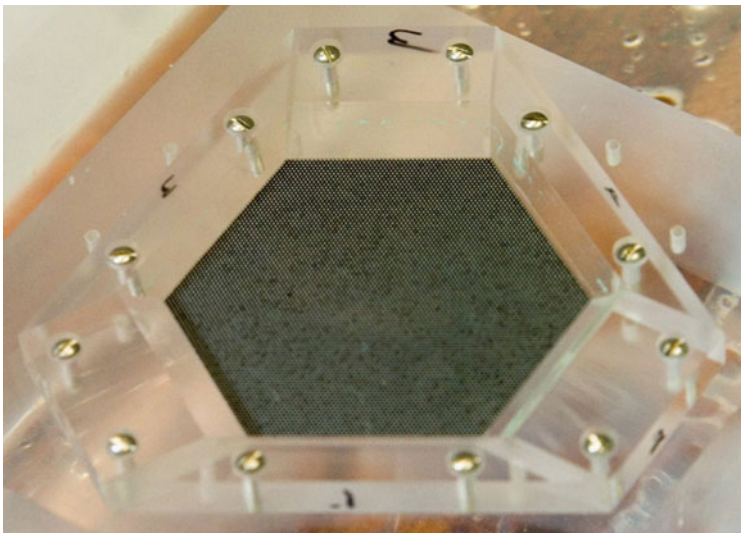

Fig. 4.10 3D single phononic crystal assembled in the supporting template

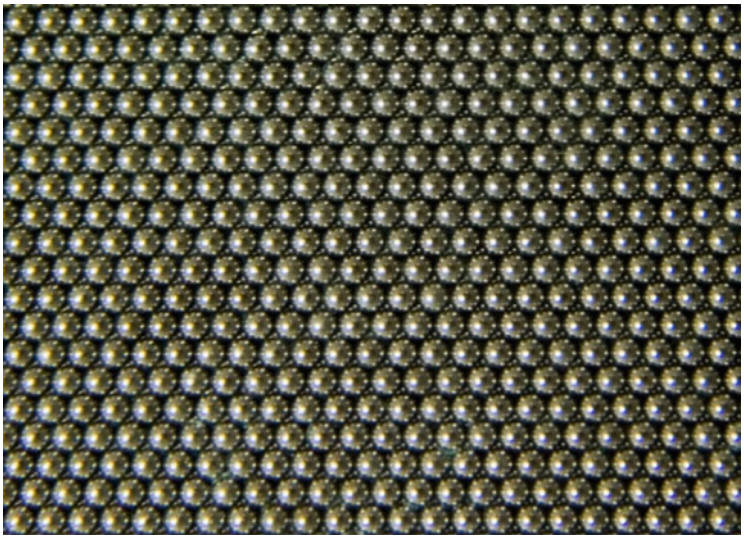

Fig. 4.11 Close-up view of the surface of the crystal, which is shown in Fig. 4.10

4.2.2.1 Transmission Experiments

In transmission experiments one measures the coherent ballistic pulse emerging from the output side of the sample after a short pulse (often with a Gaussian

envelope) was normally incident on the input side. Usually, crystals with two flat surfaces are used and crystal properties are investigated along the directions for which the direction of the output pulse is not expected to change with respect to that of the input pulse. In this case the far-field waveforms are spatially uniform in a plane parallel to the crystal faces, and thus the outgoing pulse can be accurately detected using a planar transducer, whose active element's characteristic dimensions are many times larger than the wavelength of the measured pulse. (The diffraction orders that appear at high frequencies are effectively eliminated by measuring the transmitted field over the finite transverse width that is set by the diameter of the detecting transducer.) Such a transducer averages any field fluctuations (for example due to imperfections inside the sample) and provides information on the average transport properties of the crystal. Another benefit of such averaging is an increase of the signal-to-noise ratio. Note also that to ensure the best possible approximation of the incident pulse by a plane wave, the sample should be placed in the far-field of the generating transducer. In the ultrasonic frequency range, the most convenient reference material in which the transducers and crystal can be located is water.

The analysis of the recorded pulse is done by comparing it with a reference pulse, obtained by recording a pulse propagating directly between generating and receiving transducers (with the sample removed from the experimental set-up). To allow the transmission properties to be determined from a direct comparison between the reference and measured pulses, the reference pulse should be shifted by the time $\Delta t = L/\upsilon_{\text{wat}}$, where L is the crystal thickness and υ_{wat} is the speed of sound in the medium between source and receiver. Since the attenuation in water is negligibly small, the time-shifted reference pulse accurately represents the pulse that is incident on the input face of the sample.

Figures 4.12a and 4.12b shows a typical example of incident and transmitted pulses for a 3D phononic crystal of tungsten carbide beads in water. The effects on the transmitted pulse of multiple scattering inside the crystal are clearly seen by the considerable dispersion of the pulse shape. Since the full transmitted wave function is measured, complete information on both *amplitude* and *phase* can be determined using Fourier analysis. The amplitude transmission coefficient as a function of frequency is given by the ratio of the magnitudes of the Fourier transforms of the transmitted and input pulses:

$$T(f) = \frac{A_{\text{trans}}(f)}{A_{\text{ref}}(f)} \tag{4.2}$$

Figure 4.12c shows the Fourier transform magnitudes corresponding to the pulses in Figs. 4.12b and 4.12b, demonstrating not only the large effect that phononic crystals can have on the amplitude of transmitted waves but also the wide range of frequencies that can be probed in a single pulsed measurement.

In addition to the transmission coefficient, ballistic pulse measurements also provide information on the transmitted phase, from which the wave vector can be obtained. This phase information is also directly related to the phase velocity υ_{phase}

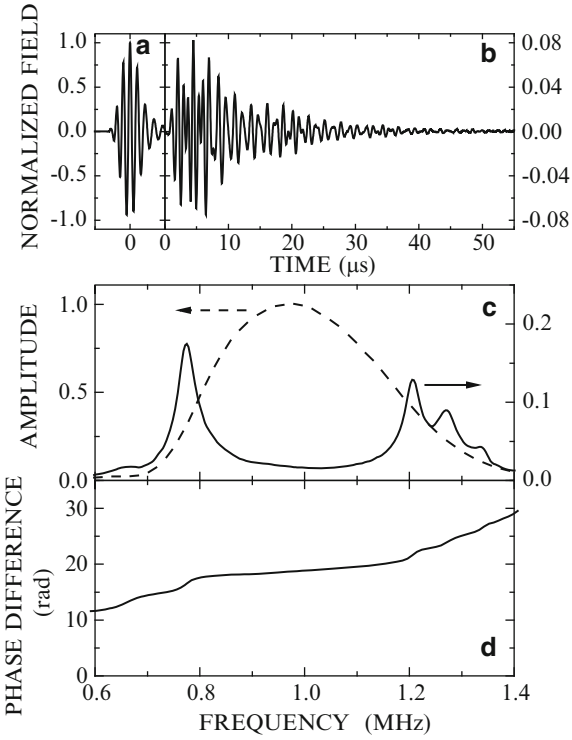

Fig. 4.12 (**a**) Incident and (**b**) transmitted ultrasonic pulses through a 6-layer 3D phononic crystal of tungsten carbide beads in water. The crystal structure is FCC, and the direction of propagation is along the [111] direction. (**c**) The amplitude of the incident (*dashed line*; left axis) and transmitted pulses (*solid line*; right axis), obtained from the fast Fourier transforms of the waves in (**a**) and (**b**). Their ratio yields the frequency dependent transmission coefficient [(4.2)]. (**d**) The phase difference between the transmitted and reference pulses, from which frequency dependence of the wave vector can be determined [(4.3)]. The large decrease in transmitted amplitude near 1 MHz and the nearly constant phase difference of $n\pi$, where $n = 6$ is the number of layers in the crystal, are characteristics of a Bragg gap

of the component of the Bloch state with wave vector in the extended zone scheme. These parameters are measured by analyzing the cumulative phase difference $\Delta\varphi$ between transmitted and input pulses (obtained from Fourier transforms of both signals—see Fig. 4.12d). This phase difference can be expressed as follows:

$$\Delta\varphi = kL = \frac{2\pi L}{\upsilon_{\text{phase}}} f \tag{4.3}$$

where L is the crystal thickness. The ambiguity of 2π in the phase can be eliminated by making measurements down to sufficiently low frequencies, since the phase difference must approach zero as the frequency goes to zero. From (4.3) it is possible to obtain directly the wave vector as function of frequency in the extended

zone scheme; the corresponding wave vector in the reduced zone scheme is obtained by subtracting the appropriate reciprocal lattice vector. Thus, (4.3) allows the dependence of the angular frequency ω on the wave vector k to be determined, yielding the dispersion curve and hence the band structure.

Finally, the experiments on the transmission of ballistic pulses allow the group velocity, which is the velocity of Bloch waves in the crystal, to be measured. By its definition, the group velocity is the velocity with which a wave packet travels as a whole. Since the transmitted pulse may get distorted from its original Gaussian shape as it passes through the crystal, especially if the pulse bandwidth is wide (as in Fig. 4.12), the group velocity may lose its meaning in this case [10]. However, it is still possible to recover two essentially Gaussian pulses by digitally filtering the input and output pulses with a narrow Gaussian bandwidth centered at the frequency of interest. The group velocity at that frequency is then found by the ratio of the sample thickness L to the time delay Δt_g between two filtered pulses:

$$\upsilon_{\mathrm{g}} = L/\Delta t_{\mathrm{g}}. \tag{4.4}$$

This direct method of measuring the group velocity is illustrated by Fig. 4.13, which shows input and transmitted pulses filtered at the central frequency of 0.95 MHz with a bandwidth of 0.05 MHz, for a 12-layer 3D crystal of tungsten carbide beads in water. The delay time is also indicated. By repeating this procedure for different frequencies, the frequency dependence of the group velocity can be found.

4.2.2.2 Field Mapping Experiments

In certain cases, the outgoing field is not expected to be spatially uniform and the direction of the outgoing pulse might not be perpendicular to the crystal's output face (as in focusing and negative refraction experiments). To investigate the field distribution a transducer whose size is larger than the wavelength cannot be used as it smears out the spatial variations of the field by detecting the average pressure across the transducer face. To resolve subwavelength details and map the field accurately one needs an ultrasound detector with physical dimensions less than a wavelength. For example, Yang et al. [7] and Sukhovich et al. [5] used a small hydrophone with an active element diameter of 0.4 mm to investigate spatial properties of the output sound field. This detector was appropriate since in their experiments the wavelength in water ranged from 0.5 to 3 mm. In practice, the ultrasound field was measured at every point of a rectangular grid by mounting the hydrophone on a 3D motorized translation stage. In case of the experiments by Sukhovich et al. [5], the plane of the grid was perpendicular to the rods and intersected them approximately in their mid-points (to avoid edge effects). Fig. 4.14 illustrates the experimental geometry used to map the outgoing field in negative refraction experiments with the prism-shaped crystal.

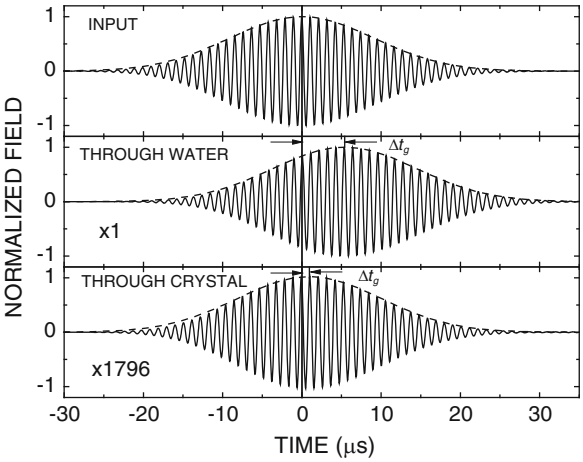

Fig. 4.13 The group velocity is measured directly from the time delay Δt_g between the peaks of the filtered input and transmitted pulses for a sample of given thickness L. The *bottom* and *middle panels* compare pulses with a bandwidth of 0.05 MHz transmitted through a 12-layer 3D phononic crystal of tungsten carbide beads in water and through the same thickness of water. Relative to the input pulse (*top panel*), the time delay for the transmitted pulse through the crystal is much shorter than through water, showing directly that large values of the group velocity are measured in this phononic crystal at this frequency, which falls inside the first bandgap. The pulses are normalized to unity for ease of comparison, with the normalization factors being indicated in the figures. The *dashed lines* indicate that the Gaussian envelope of the input pulse is well preserved for both transmitted pulses

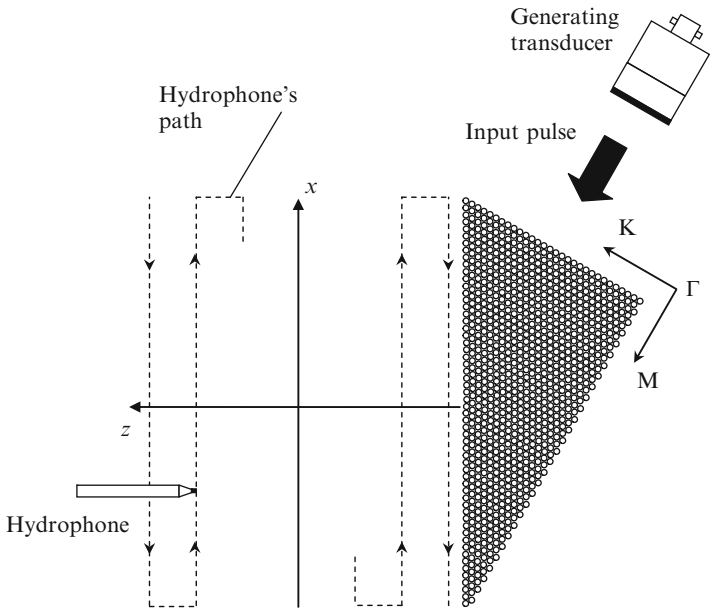

Fig. 4.14 Field mapping to investigate negative refraction for a prism-shaped 2D phononic crystal

The recorded waveforms (acquired at each point of the grid) can be analyzed in either time or frequency domains. In the time domain, the value of the field at each grid point is read at some particular time and then used to create an image plot, which is essentially a snapshot of the field at this particular moment of time. By creating several image plots for different times, one can also investigate the time evolution of the transmitted sound. The video in the supplementary information to [5] shows an example of such time-evolving field maps. In the frequency domain, one first calculates the Fourier transforms (FTs) of the acquired waveforms. The magnitude of each FT is read at a single frequency and these values are used to make the image plot. The image plot in this case represented an amplitude map (proportional to the square root of intensity), which would be obtained from the field plot if continuous monochromatic wave were used as an input signal instead of a pulse. Examples of field and amplitude distributions measured in the negative refraction and focusing experiments by Sukhovich et al. [5, 11] are shown in Sects. 4.4 and 4.5.

4.3 Band Gaps and Tunneling

Lattice periodicity in phononic crystals leads to large dispersive effects in wave transport, which are shown by band structure plots that depict the relationship between frequency and wave vector along certain high symmetry directions. Representative examples of the band structures of 2D and 3D phononic crystals are illustrated in Figs. 4.15 and 4.16 for the structures described in Sect. 4.1. In both these examples, the continuous medium surrounding the inclusions is water, with the scattering inclusions being 1.02-mm-diameter steel rods for the 2D case and 0.800-mm-diameter tungsten carbide spheres for the 3D case. The solid curves in these figures show the band structures calculated using Multiple Scattering Theory (MST), which is ideally suited for determining the band structures of mixed crystals consisting of solid scatterers embedded in a fluid matrix (see Chap. 10). The symbols represent experimental data, determined from measurements of the transmitted cumulative phase $\Delta\phi$, as described in the previous section. To compare with the theoretical band structure plots, the measured wave vectors ($k = \omega/v_p = \Delta\phi/L$) are folded back into the first Brillouin zone by subtracting a reciprocal lattice vector ($\mathbf{k}_{\text{reduced}} = \mathbf{k}_{\text{extended}} - \mathbf{G}$). Excellent agreement between theory and experiment is seen, showing that experiments on relatively thin samples (6 layers for the 2D case, and 12 layers for the 3D case) are sufficient to reveal the dispersion relations of waves in the pass bands of an infinite periodic medium.

For both phononic crystals, there is a large velocity and density difference between the scattering inclusions and the continuous embedding medium, facilitating the formation of band gaps due to Bragg scattering. It is well known that Bragg gaps are caused by destructive interference of waves scattered from planes of periodically arranged scatterers. The lowest frequencies at which such band gaps may occur satisfy the condition that the separation between adjacent

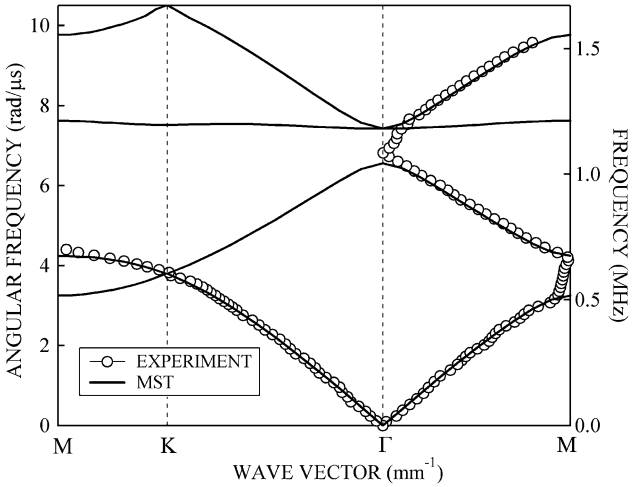

Fig. 4.15 Band structure of a 2D phononic crystal of 1.02-mm-diameter steel rods arranged in a triangular lattice and surrounded by water. The lattice constant $a = 1.27$ and the steel volume fraction is 0.584. *Solid curves* are predictions of the MST and *open circles* are experimental data. There are no data points for the second band along ΓK as this is a "deaf" band to which an incident plane wave cannot couple

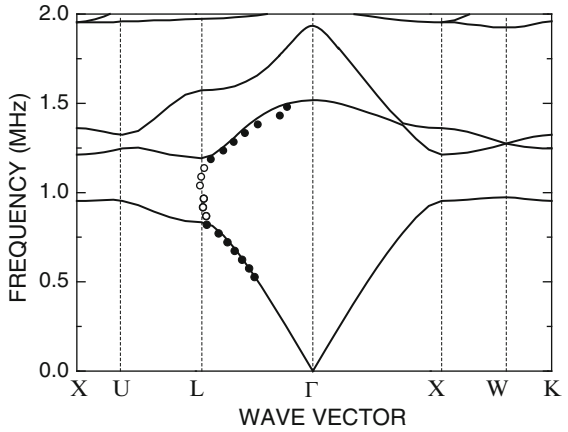

Fig. 4.16 Band structure of a 3D phononic crystal made from 0.800-mm-diameter tungsten carbide spheres arranged in the FCC lattice and surrounded by water at a volume fraction of 0.74. *Solid curves* are predictions of the MST and *circles* are experimental data

crystal planes is approximately half the wavelength in the embedding medium. In the 2D crystal, the lowest "gap" is only a stop band along the ΓM direction, with the lowest complete gap occurring between the 2nd and 3rd pass bands. For the 3D crystal, the lowest band gap near 1 MHz is wide and complete, with the complete

gap width being nearly 20 % and the width along the [111] direction extending to approximately 40 %. These results show that phononic crystals with relatively simple structures can exhibit wide gaps, which are easier to achieve for phononic crystals than their optical counterparts because of the ability to manipulate large scattering contrast *via* velocity and density differences. Indeed, there is an extensive literature on how to create large band gaps for phononic crystals with a wide variety of structures, with the important role of density contrast now being well established (see the special edition on phononic crystals in Zeitschrift fur Kristallographie for many examples and references [12]).

The existence of band gaps in phononic crystals of finite thickness is shown clearly through measurements of the transmission coefficient. Results for the 2D and 3D crystals are plotted in Figs. 4.17 and 4.18, where the symbols represent experimental data and the solid curves are theoretical predictions using the layer MST [5, 9]. At low frequencies below the first band gap, the transmission exhibits small oscillations due to an interference effect resulting from reflections at the crystal boundaries; there are $n-1$ oscillations, where n is the number of layers, and the peaks in these oscillations correspond to the low frequency normal modes of the crystal. At band gap frequencies, the amplitude transmission coefficient shows very pronounced dips which became deeper in magnitude as the number of layers in the crystal increases. The sample-thickness dependence of the transmission coefficient in the middle of the gap (at 0.95 MHz) is plotted for the 3D crystals in Fig. 4.19. This figure shows that the transmitted amplitude A decreases exponentially with thickness in the gap, $A(L) = A_0 \exp[-\kappa L]$, consistent with evanescent decay of the amplitude, with κ being the imaginary part of the wave vector. The value of κ is 0.93 mm^{-1} in the middle of the gap, quantifying how quickly the transmission drops as the thickness increases. Thus, wave transport crosses over from propagation with virtually no losses outside the gap to evanescent transmission inside the gap. This evanescent character of the transmission at gap frequencies suggests that ultrasound is transmitted through crystals of finite thickness by tunneling, whose dynamics can be investigated by measuring the group velocity v_g and predicting its behavior using the MST [6]. Figure 4.20 shows that the group velocity increases linearly with sample thickness in the absence of dissipation (solid line), an unusual result that is the classic signature of tunneling in quantum mechanics [13], implying that the group time ($t_g = L/v_g$) is independent of thickness in sufficiently thick samples. This behavior is clearly seen in Fig. 4.20 by the theoretical predictions without absorption for thicknesses greater than 5 layers of beads. The dashed line in this figure implies a constant value of the tunneling time through the phononic crystal given by $t_g = 0.54$ μs, as expected for tunneling when $\kappa L \gg 1$. The experimentally measured group velocities are less than this theoretical prediction but are still remarkably fast, being greater than the speed of sound in water (1.5 mm/μs) for all crystal thicknesses, and greater than the velocities of elastic waves in tungsten carbide (6.66 and 3.23 mm/μs for longitudinal and shear waves, respectively) for the largest thicknesses. These experimental results for v_g are smaller than the dashed line in Fig. 4.20 because of absorption, which can be taken into account in the MST by allowing the moduli of the constituent materials

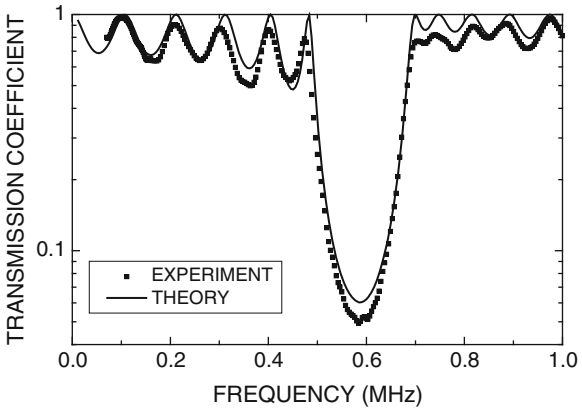

Fig. 4.17 Amplitude transmission coefficient as a function of frequency for a 6-layer 2D phononic crystal along the ΓM direction. *Squares* and *lines* represent experimental data and MST predictions, respectively

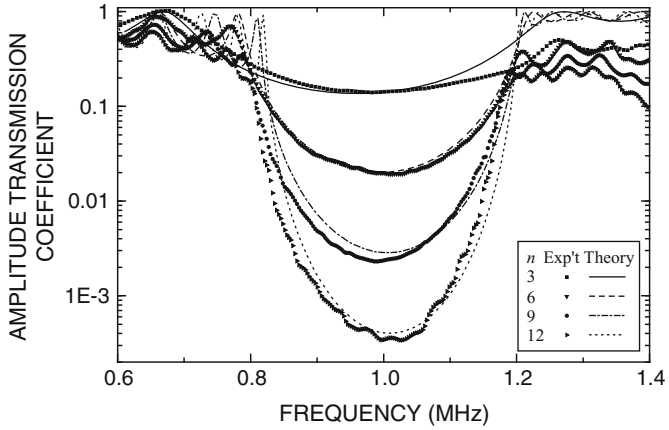

Fig. 4.18 Amplitude transmission coefficient as a function of frequency for 3-, 6-, 9- and 12-layer 3D phononic crystals of tungsten carbide beads in water along the ΓL direction. *Symbols* and *lines* represent experimental data and MST predictions, respectively

to become complex. The predictions of the theory with absorption are shown by the dashed curve and give a satisfactory description of the experimental results, indicating how dissipation, which has no counterpart in the quantum tunneling case, significantly affects the measured tunneling time.

The effect of dissipation on tunneling was interpreted using the two-modes model (TMM), which allows the role of absorption to be understood in simple physical terms [6]. Absorption in the band gap of a phononic crystal cuts off the long multiple scattering paths, making the destructive interference that gives rise to the band gap incomplete. As a result, a small-amplitude propagating mode exists in

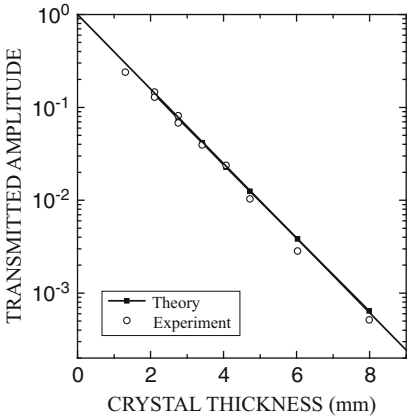

Fig. 4.19 Amplitude transmission coefficient as a function of thickness in the middle of the Bragg gap at 0.95 MHz for FCC phononic crystals of tungsten carbide beads in water

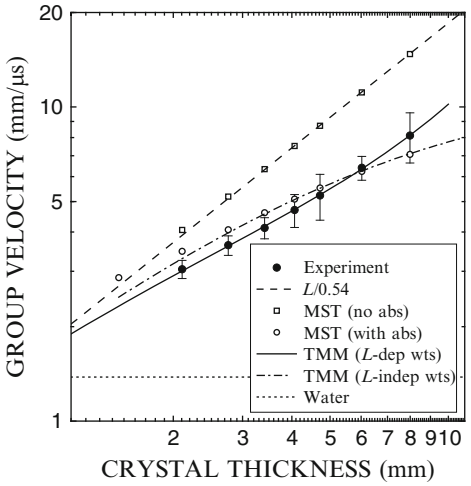

Fig. 4.20 Group velocity as a function of thickness in the middle of the Bragg gap at 0.95 MHz for FCC phononic crystals of tungsten carbide beads in water

parallel with the dominant tunneling mode, so that the group velocity can be calculated from the weighted average of the tunneling time t_{tun} and the propagation time $t_{\text{prop}} = L/v_{\text{prop}}$. Thus, $\bar{v}_{\text{g}} = L/\left(w_{\text{tun}}t_{\text{tun}} + w_{\text{prop}}L/v_{\text{prop}}\right)$, where w_{tun} and w_{prop} are the weighting factors, which depend on the coupling coefficients and attenuation factors of each mode [6, 14]. The best fit to the data, shown by the solid curve in Fig. 4.20, was obtained with a coupling coefficient to the tunneling mode of 0.95, confirming the dominance of the tunneling mechanism, and with a contribution from the propagating component that diminished gradually with thickness, consistent with decreased dissipation in the thicker crystals—a physically reasonable result [14]. It is also interesting to note that with thickness-independent weight factors, the predictions of the TMM and the MST with absorption are very similar. These results

show that the TMM successfully account for the effects of absorption on the tunneling of ultrasonic waves in phononic crystals, thereby providing a simple physical picture of the underlying physics.

The demonstration of the tunneling of ultrasound through the band gap of a phononic crystal raises an interesting question: Can resonant tunneling, analogous to the resonant tunneling of a particle through a double barrier in quantum mechanics, be observed in phononic crystals? This effect is intriguing since on resonance the transmission probability of a quantum particle through a double barrier is predicted to be unity, even though the transmission probability through a single barrier is exponentially small. This question has been addressed through experiments and theory on the transmission of ultrasound through pairs of phononic crystals separated by a uniform medium, which formed a cavity between them [8]. Evidence for resonant tunneling was revealed by large peaks in the transmission coefficient on resonance, which occurs at frequencies in a band gap when the cavity thickness approaches a multiple of half the ultrasonic wavelength. However, the transmission was less than unity on resonance because of the effects of dissipation in the phononic crystals, an effect that has a simple interpretation in the two modes model as a consequence of leakage due to the small propagating component in the band gap. Thus, the subtle effects of absorption on resonant tunneling in acoustic systems could also be studied. In addition, the use of pulsed experiments enabled the dynamics of resonant tunneling to be investigated. Very slow ("subsonic") sound was observed on resonance, while at neighboring frequencies, very fast ("supersonic") speeds were found. In contrast to the quantum case, ultrasonic experiments on resonant tunneling in double phononic crystals enable the full wave function to be measured, allowing both phase and amplitude information, in addition to static and dynamic aspects, to be investigated.

While the most commonly studied type of band gap in phononic crystals arises from Bragg scattering, band gaps may also be caused by mechanisms, such as hybridization and weak elastic coupling effects, which do not rely on lattice periodicity. Hybridization gaps are caused by the coupling between scattering resonances of the individual inclusions and the propagating modes of the embedding medium [15]. Their origin may be viewed as a level repulsion effect. Band gaps due to this hybridization mechanism were first observed, and have also been studied more recently, in random dispersions of plastic spheres in a liquid matrix [16–20]. Such gaps are of particular importance in the context of acoustic and elastic metamaterials, where the coupling of strong low frequency resonances with the surrounding medium may lead to negative values of dynamic mass density and modulus [21]. In phononic crystals, it is the possibility of designing structures in which both hybridization and Bragg effects occur in the same frequency range that is especially interesting [22]. For example, the combination of Bragg and hybridization effects has been invoked to explain the remarkably wide bandgaps that have been found both experimentally and theoretically in three dimensional (3D) crystals of dense solid spheres (e.g., steel, tungsten carbide) in a polymeric matrix (e.g., epoxy, polyester) [14, 23]. Other examples of band gaps that are enhanced by the combined effects of resonances and Bragg scattering have been

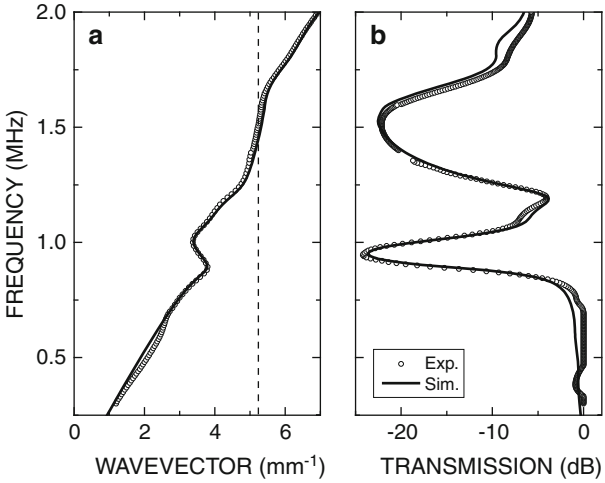

Fig. 4.21 Dispersion relation (**a**) and transmission coefficient (**b**) for a 6-layer 2D crystal of nylon rods in water at a nylon volume fraction of 0.40. *Symbols* and *solid curves* represent experimental data and finite element simulations respectively. The lower band gap near 1 MHz is an example of a pure hybridization gap, characterized by a sharp dip in transmission and a range of frequencies in the dispersion curve for which the group velocity is negative. The broader second gap centered near 1.5 MHz has the character of a Bragg gap, with a large positive group velocity, and occurs at the edge of the first Brillouin zone, indicated by the *vertical dashed* line

demonstrated in two-dimensional crystals of glass rods in epoxy and three dimensional arrays of bubbles in a PDMS matrix [24, 25].

We illustrate the characteristic features of hybridization gaps by showing results of experiments and finite element simulations on a two-dimensional hexagonal phononic crystal of nylon rods in water [26]. Figure 4.21 shows the dispersion relation and transmission coefficient in the vicinity of the lowest scattering resonance of nylon rods for a crystal with a nylon volume fraction of 40 %. The resonance occurs near 1 MHz for the 0.46-mm-diameter rods used in this crystal. Near this frequency, the dispersion relation exhibits a negative slope, corresponding to a range of frequencies with negative group velocity. Direct measurements of the negative group velocity were performed from transmission experiments using narrow-bandwidth pulses in the time domain, where the peak of the transmitted pulse was observed to exit the crystal before the peak of the input pulse entered the crystal. The negative time shift arises from pulse reshaping due to anomalous dispersion and does not violate causality. This property of negative group velocity is characteristic of resonance-related band gaps, and can be used to distinguish them from Bragg gaps, for which the group velocity is large and positive, as shown above. At higher frequencies, a second gap is observed for this crystal near 1.5 MHz; this gap is dominated by Bragg effects, with large positive group velocities inside the gap.

A third mechanism leading to the formation of band gaps occurs in three-dimensional single-component phononic crystals with the opal structure: spherical

particles that are bonded together by sintering to form a solid crystal without a second embedding medium. Band gaps in such phononic crystals have been observed at both hypersonic and ultrasonic frequencies [26, 27]. They have also been seen in disordered structures of randomly positioned sintered spherical particles [28, 29]. The origin of the band gaps is associated with resonances of the spheres, but the underlying mechanism is quite different to the formation of hybridization gaps. Indeed the physics is more analogous to the tight-binding model of electronic band structures, with the resonant frequencies of the spheres corresponding to the electronic energy levels of the atoms. The coupling between the individual resonances of the spherical particles, due to the necks that form between the particles during sintering, leads to the formation of bands of coupled resonances with high transmission (pass bands). However, if the mechanical coupling between the spheres is sufficiently weak, these pass bands have limited bandwidth, and band gaps form in between them. These band gaps can be quite wide and are omnidirectional.

Up to now, the theory and experiments we have described in this chapter have been related to absolute band gap properties of phononic crystals. These results on sound attenuation and tunneling have proved phononic crystals meaningful in the perspective of building-up artificial materials with frequency dependent properties. However, the periodic structure of phononic crystals similarly impacts propagation of elastic waves in the frequency range of the passing bands. More specifically, the zone folding effects imply the existence of negative group velocity bands. Such bands offer the opportunity of negative refraction. In the next sections, theoretical and practical aspects of negative refraction are discussed.

4.4 Negative Refraction in 2D Phononic Crystals

The periodicity of the phononic crystals makes them markedly different from the homogeneous materials since wave propagation now depends on the direction inside the crystal. It was shown in the previous section that the periodicity is the fundamental cause for the existence of the stop bands and band gaps. In this section, we will consider some other remarkable properties of phononic crystals not found in regular materials: negative refraction and sound focusing. It will be shown that both phenomena are essentially *band structure* effects.

It is well known that reflection and refraction of waves of any nature (acoustic, elastic or electromagnetic) occurring at the interface between two different media are governed by *Snell's* law. According to Snell's law, the component of the wavevector, which is tangential to the interface, must be *conserved* as the wave propagates from one medium to another. Let us consider, for example, the simple case of a plane wave obliquely incident from a liquid with Lamé coefficients λ_1 and $\mu_1 = 0$ on an isotropic solid characterized by Lamé coefficients λ_2 and μ_2 (Fig. 4.22). As a result of the wave interaction with the boundary, part of the energy of the incident wave is reflected back into the liquid in the form of a reflected

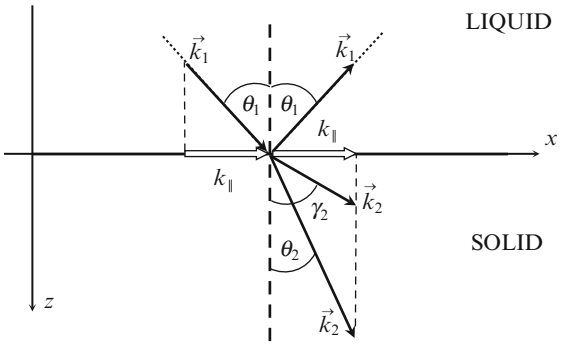

Fig. 4.22 Reflection and refraction of a plane wave incident obliquely on the liquid/solid interface from the liquid. Note the conservation of the wavevector component $k_{||}$

wave, which propagates with the phase velocity $c_1 = \sqrt{\lambda_1/\rho}$. The rest of the incident wave is transmitted into the solid and generates two outgoing waves, longitudinal and transverse, which propagate with phase velocities $c_2 = \sqrt{(\lambda_2 + 2\mu_2)/\rho}$ and $b_2 = \sqrt{\mu_2/\rho}$ respectively. Snell's law requires that parallel (to the interface) components of the wavevectors of the incident wave, $k_1 = \omega/c_1$, and of both refracted waves, $k_2 = \omega/c_2$ and $k_{2t} = \omega/b_2$ be equal (note that k_1 lies in the x–z plane and so do k_2 and k_{2t}). Mathematically, this means that the following conditions must be satisfied:

$$k_1 \sin\theta_1 = k_2 \sin\theta_2 = k_{2t} \sin\gamma_2 \tag{4.5}$$

where angles θ_1, θ_2 and γ_2 are indicated in Fig. 4.22. By introducing the notion of the index of refraction n and n', where $n = k_2/k_1$ and $n' = k_{2t}/k_1$, Snell's law is frequently written in the following form:

$$\begin{aligned} \sin\theta_1 &= n \sin\theta_2 \\ \sin\theta_1 &= n' \sin\gamma_2 \end{aligned} \tag{4.6}$$

With the help of Snell's law (4.5), one can easily calculate the refraction angles θ_2 and γ_2 when the parameters of the two media and the angle of incidence θ_1 are known (it is clear from Snell's law that the angle of reflection must be equal to the angle of incidence). Physically, Snell's law implies that refraction and reflection occur in the same way at any point of the interface between two media (i.e., independent of the x coordinate in Fig. 4.22).

The refraction of the wave from one medium to another can be conveniently visualized with the help of the *equifrequency* surfaces (or contours in case of 2D systems). Equifrequency surfaces are formed in k-space by all points whose wavevectors correspond to plane waves of the same frequency ω. Physically, they display the magnitude of the wavevector $\vec{k}$ of a plane wave propagating in the given medium as a function of the *direction* of propagation. For any isotropic medium the equifrequency surfaces are perfect spheres (circles in 2D), since the

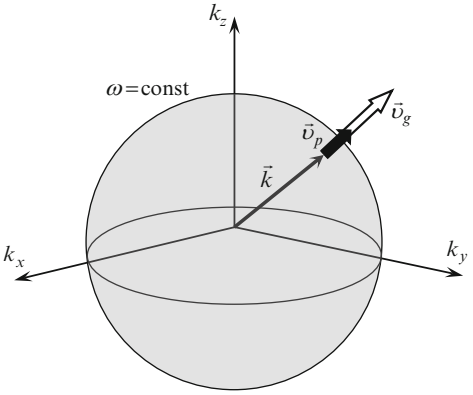

Fig. 4.23 Equifrequency surface of an isotropic medium

magnitude of the wavevector is independent of the direction of propagation, as illustrated in Fig. 4.23.

Another extremely important property of equifrequency surfaces is that at its every point the direction of the group velocity $\vec{v}_g$ (or equivalently the direction of the energy transport) in the medium at a given frequency coincides with the direction of the normal to the equifrequency surface (pointing towards the increase of ω). In other words, $\vec{v}_g$ is given by the gradient of ω as a function of the wavevector $\vec{k}$:

$$\vec{v}_g = \vec{\nabla}_{\vec{k}}\omega(\vec{k}) \tag{4.7}$$

On the other hand, the direction of the phase velocity $\vec{v}_p$ (or the direction of the propagation of constant phase) is set by the direction of the wavevector $\vec{k}$. As shown in Fig. 4.23, in an isotropic medium both phase and group velocities point in the same direction. This is however not the case in an *anisotropic* medium (e.g., GaAs or CdS), in which magnitude of the wavevector is direction dependent and thus equifrequency surfaces will not be perfect spheres anymore.

Having introduced the notion of the equifrequency surfaces/contours, let us use them to illustrate the refraction of a plane wave in Fig. 4.24. This is accomplished by drawing the equifrequency contours (since all wavevectors lie in the x–z plane) for each medium on the scale that would correctly represent the relative magnitudes of the wavevectors of the incident and refracted waves. By projecting the parallel component of the incident wavevector $\vec{k}_1$ (which must be conserved according to Snell's law) on the contours of the solid, one is able to find the direction of propagation (i.e., refraction angles) of both waves in the solid (Fig. 4.24). As was explained in the preceding paragraph, group velocities $\vec{v}_g$ and wavevectors $\vec{k}$ are *parallel* to each other (because of the spherical shape of the equifrequency contours) and also point in the *same* direction, since ω increases as the magnitude of the wavevector increases, meaning that $\vec{\nabla}_{\vec{k}}\omega(\vec{k})$ points along the *outward* normal to the equifrequency contour. The significance of the last observation will become apparent when the refraction in 2D phononic crystals will be discussed.

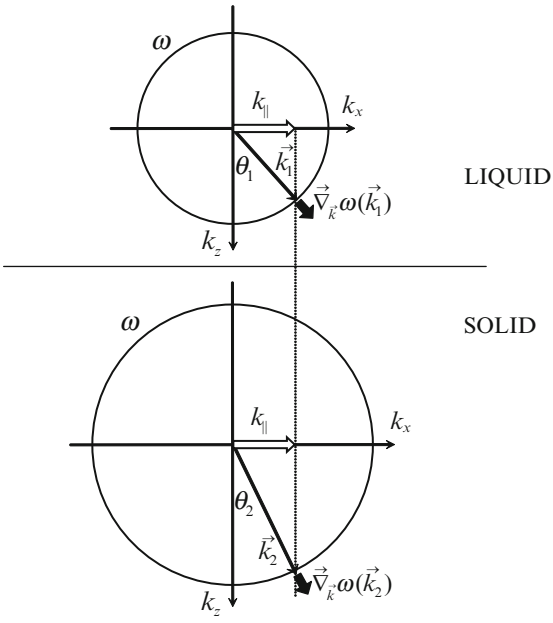

Fig. 4.24 Refraction of a plane wave in Fig. 4.1 is illustrated with the help of the equifrequency contours (the same diagram holds for the transverse wave, which is omitted for simplicity)

The periodicity of the phononic crystal makes it an anisotropic medium, in which the magnitude of the wavevector depends on the direction inside the crystal and equifrequency contours are, in general, not circular. However, the frequency ranges still might exist where the equifrequency are almost perfect circles as is the case of a 2D crystal made of solid cylinders assembled in a triangular crystal lattice in a liquid matrix. For example, for a crystal made of stainless steel rods immersed in water the MST predicts the existence of circular equifrequency contours in the 2nd band for the frequencies that are far enough from the Brillouin zone edges (ranging from 0.75 MHz to 1.04 MHz, which is the top frequency of the 2nd band). The equifrequency contours for the several frequencies are presented in Fig. 4.25 [5].

Note that in this frequency range the wavevector $\vec{k}_{\mathrm{cr}}$ and the group velocity $\vec{v}_{\mathrm{g}}$ (which defines the direction of the energy transport inside the crystal) are *antiparallel* to each other. This is the consequence of the fact that ω increases with the *decreasing* magnitude of the wavevector, meaning that $\vec{\nabla}_{\vec{k}}\omega(\vec{k})$ points along the *inward* normal to the equifrequency contour, as explained in Fig. 4.26. It is also obvious that, because of the circular shape of the equifrequency contours in the 2nd band, $\vec{k}_{\mathrm{cr}}$ and $\vec{v}_{\mathrm{g}}$ are antiparallel *irrespective* of the direction inside the crystal.

Let us investigate the consequence of this fact by considering the refraction into such a phononic crystal of a plane wave incident on the liquid/crystal interface from the liquid and having frequency lying in the 2nd band of the crystal (Fig. 4.27). The parallel component of the wavevector in both media must be conserved just as it was in the case displayed in Fig. 4.24. What is different however is that the wave vector inside the crystal and the direction of the wave propagation inside the crystal

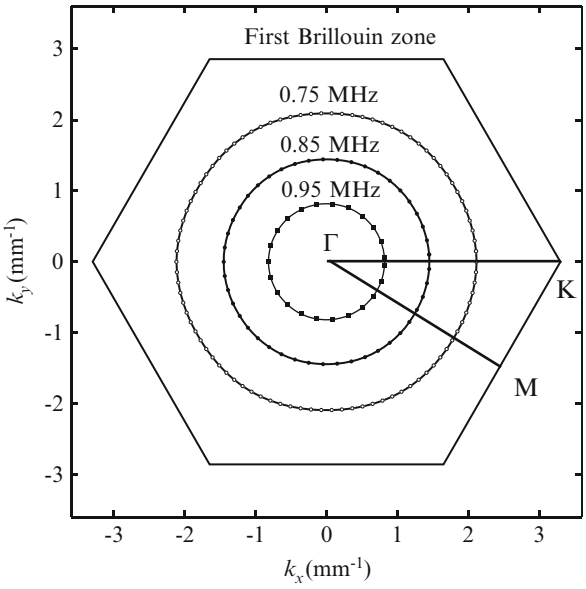

Fig. 4.25 Equifrequency contours predicted by the MST for the several frequencies in the 2nd band of the 2D phononic crystal made of stainless steel rods in water

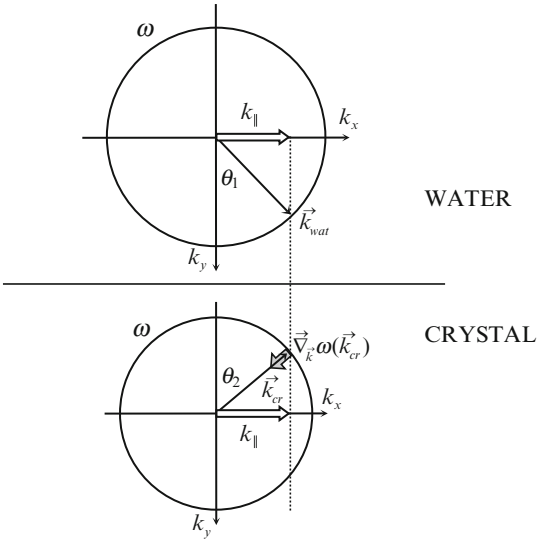

Fig. 4.26 Refraction of a plane wave at the water/crystal interface. The choice of the upward direction of the wavevector $\vec{k}_{cr}$ provides a wave propagating inside the crystal

are now *opposite* to each other. As a result, both incident and refracted waves (rays) stay on the *same* side of the normal to the water/crystal interface (compare with Fig. 4.24 in which incident wave crosses the plane though the normal as it refracts into the lower medium).

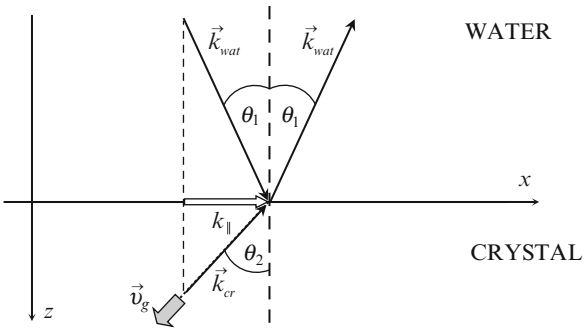

Fig. 4.27 Negative refraction of a plane wave incident obliquely on the water/crystal interface. Note the conservation of the wavevector component $k_{||}$

Since the refracted wave happens to be on the negative side of the normal, this unusual refraction can also be described by assigning an effective *negative* index of refraction to the crystal. In this case we say that the incident wave is *negatively* refracted into the crystal and use the term "*negative* refraction" to indicate this phenomenon. Before we proceed further with discussion of sound wave refraction in phononic crystals, it is worth noting that the negative refraction considered above is fundamentally different from negative refraction in double negative materials, as originally envisaged for electromagnetic waves by Veselago [30] in materials with negative values of both electric permittivity ε and magnetic permeability μ. Although both phenomena look similar, it is a *band structure* effect in case of phononic crystals whereas in case of doubly negative materials it is brought about by the negative values of the *local* parameters of the medium (ε and μ for the electromagnetic wave case). It is also important to recognize that the negative direction of refraction is always given by the direction of the group velocity in phononic crystals.

Let us now consider the question of the *experimental* observation of the negative refraction in phononic crystals. First, it should be mentioned, that the same effect must occur when the direction of the wave in Fig. 4.27 is reversed, i.e., when the wave is incident on the crystal/water interface from the crystal. One might contemplate an experiment in which a plane wave would be incident obliquely on a *flat* phononic crystal with *parallel* sides. According to the previous discussion, it should be refracted negatively twice before it finally appears on the output side of the crystal, as shown in Fig. 4.28.

This type of experiment, however, is not able to provide conclusive evidence of the negative refraction, as the direction of the propagation of the output wave will be the same whether it refracts negatively inside the phononic crystal or positively in a slab of a regular isotropic material (Fig. 4.28). In case of an input beam of finite width, one can look for evidence of either negative or positive refraction inside the slab by measuring the position of the output beam with respect to the input beam and comparing it to the predicted value. In practice, this shift in position of the finite width beam may be difficult to resolve. Another type of experiment, which is able to

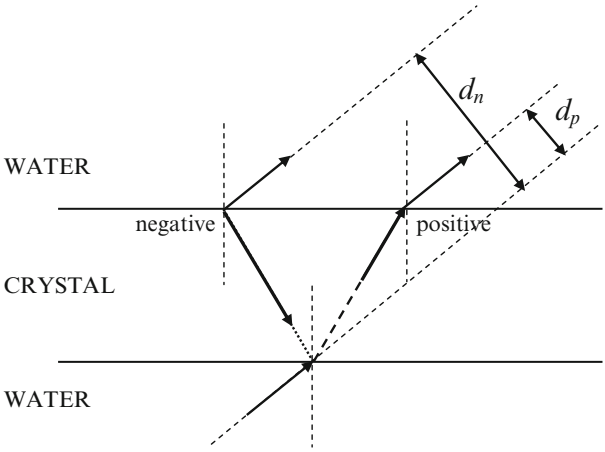

Fig. 4.28 Propagation of the sound wave through a flat crystal with parallel surfaces. Both negatively and positively refracted waves leave the crystal's surface in the same direction. Also indicated are distances d_p and d_n by which positively and negatively refracted beams are displaced with respect to the input beam.

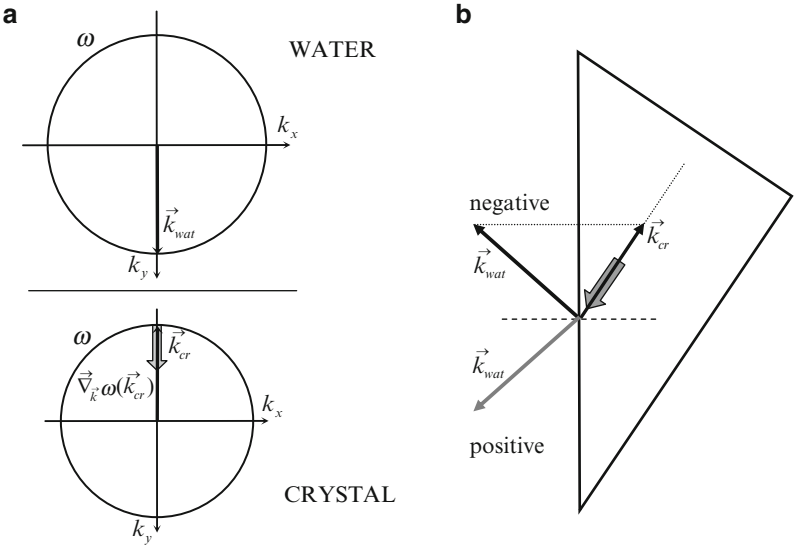

Fig. 4.29 Negative refraction experiment with the prism-shaped phononic crystal. (**a**) Equifrequency contours in water and in the crystal. In (**b**), the directions of positive and negative refraction at the output face of the prism crystal are shown. The *thick arrow* indicates the direction of wave propagation inside the crystal

provide *direct* verification of whether positive or negative refraction takes place, employs a *prism-shaped* phononic crystal (Fig. 4.29).

For the prism-shaped crystal, the input plane wave is incident normally on the shortest side of the crystal and propagates into the crystal *without* any change in its original direction, just as it would do in the case of a prism made out of a regular material (see Fig. 4.29a). Recall that the ensuing wave inside the crystal will have its wavevector $\vec{k}$ opposite to the direction of its propagation. This wave, however, will be incident *obliquely* on the output side of the crystal and must undergo negative refraction upon crossing the crystal/water interface (Fig. 4.29b), whereas in the case of a prism of a regular material the output wave will be positively refracted. Therefore, by recording on which side of the normal the outgoing wave appears as it leaves the crystal, one is able to directly observe negative refraction of the sound waves. From the predictions of the MST, one would expect the outgoing wave to emerge on the negative side of the normal. This prediction was tested in the experimentally by Sukhovich et al. [5]. The 2D phononic crystal was made in a shape of a right-angle prism which is shown in Fig. 4.30. along with the high symmetry directions of the triangular crystal lattice.

In the experiment, the input signal was normally incident on the shortest side of the crystal, and the wavefield was scanned at the output side of the crystal (Fig. 4.29b). Figure 4.31 presents the snapshot of the wavefield on which the negatively refracted outgoing wave is clearly observed.

The angle at which the negatively refracted wave emerges with respect to normal, $-21^\circ \pm 1^\circ$, was found to be in good agreement with the one predicted by the MST and Snell's law (-20.4°).

4.5 Flat Lenses and Super Resolution

In 2000, Pendry [31] has proposed to use "Double-negative" metamaterials, which means composite systems exhibiting both negative permittivity and dielectric constant, as a building material for potentially perfect lenses that beat the Rayleigh diffraction limit. This is possible thanks to the contribution of two phenomena. First intrinsic properties of negative index metamaterials provide self-focusing capabilities to a simple slab of these materials. The second effect requires the evanescent part of the spectra of a source to couple with the lens and being resonantly "amplified" in order to reach the image without losses. From this time, experimental and theoretical demonstrations of acoustic metamaterials and phononic crystals have been reported.

Early results by Yang et al. [7] in 2004 have shown the applicability of phononic structures for sound focusing. They have realized phononic crystals made of 0.8 mm-diameter tungsten carbide beads surrounded by water. The face centered cubic structure of the closed packed beads exhibits a complete band gap in the 0.98 to 1.2 MHz range. From the analysis of the equifrequency surfaces summarized in Fig. 4.32a, b, the authors have shown that significant negative refraction effects are expected due to the highly anisotropic properties of the dispersion relations.

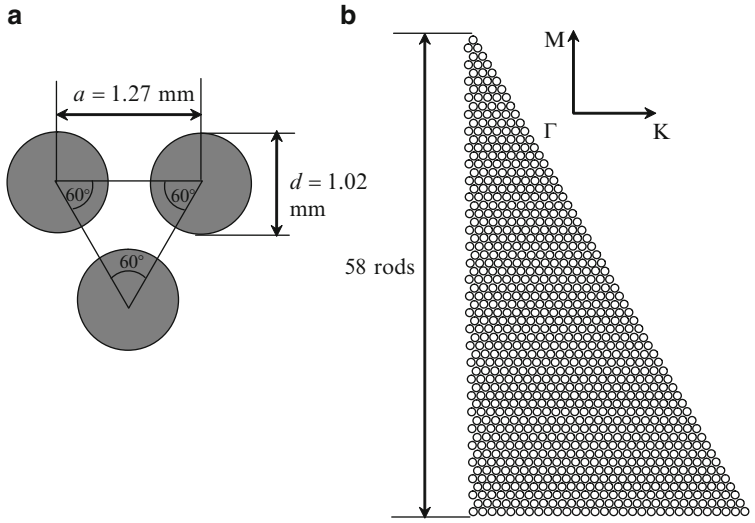

Fig. 4.30 Geometry of the 2D prism-shaped crystal. (**a**) Unit cell. (**b**) View from above. High symmetry directions, indicated as ΓM and ΓK, correspond to those shown in Fig. 4.1

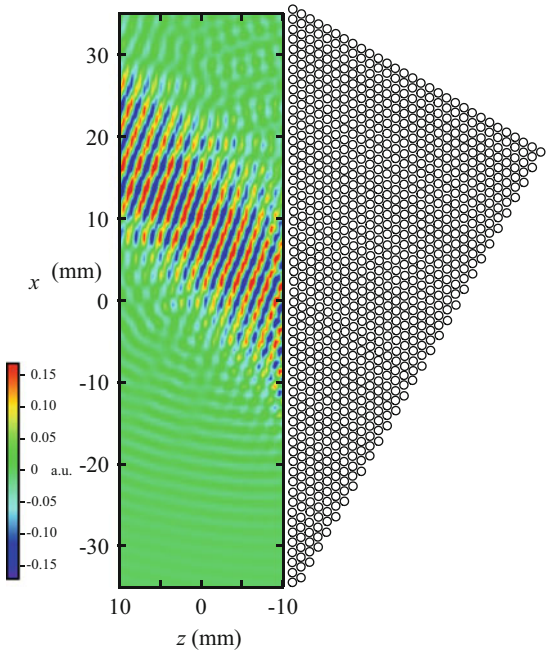

Fig. 4.31 Outgoing pulses in the negative refraction experiment (after Sukhovich et al. [5])

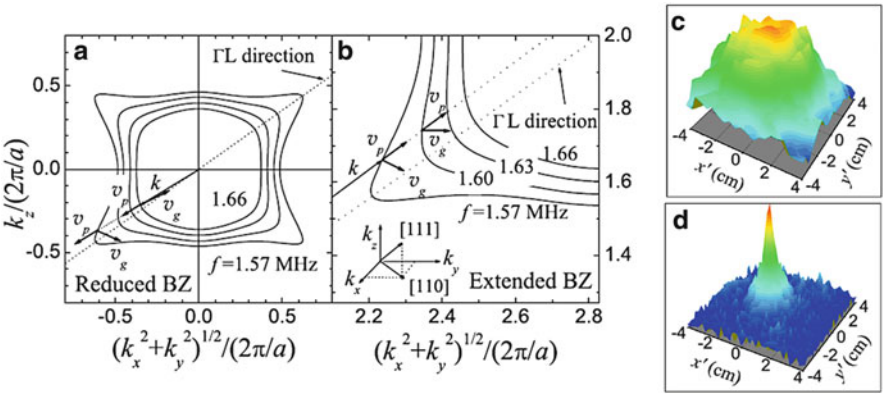

Fig. 4.32 Focusing of sound in a 3D phononic crystal after Yang et al. [7]. (**a**) Cross section of the equifrequency surfaces at frequencies near 1.60 MHz in the reduced (**a**) end extended (**b**) Brillouin zones. The cross section plane contains the [001], [110] and [111] directions. (**c**) Experimental field patterns measured a 1.57 MHz without the phononic crystal in place. (**d**) same as (**c**) with the phononic crystal in place

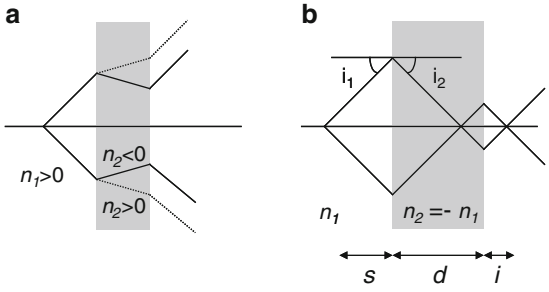

Fig. 4.33 Illustration of the refraction properties of a negative index material slab. (**a**) In the usual case of a positive material a source gives only divergent beams. If the slab is made of a negative index metamaterial then the beams are convergent in the extent of the slab. (**b**) If the slab is thick enough (or the index has sufficient magnitude), the incoming rays focus twice in the thickness of the slab and on the output side. Here the index is supposed to be opposite to the index of the embedding media. Two images are produced, inside the slab and on the output side (If the slab is too thin (Fig. 4.33a) then a single virtual image exists)

Experiments have been carried out to study the transmission of sound across a stack made of the phononic crystal mounted onto a thick substrate. As will be discussed in Fig. 4.33, negative refraction through a phononic crystal slab is expected to produce a focus inside the crystal and on the output medium. This later focus was observed by Yang et al. at the right distance on the substrate surface. They used a pinducer that produce ultrasonic pulses and a hydrophone mounted on a 3D translation stage. The recorded data was then treated by Fourier transform in

order to recover the components at the frequency of interest. The field patterns in Fig. 4.32c, d show the focusing effect in the presence of the phononic crystal.

In 2009, evidences of an acoustic super-lensing effect have been provided by Sukhovich et al. [11]. Here we describe the principles of acoustic super-resolution and go into details about these recent results.

4.5.1 Sound Focusing by a Slab of Negative Index Material

Among the numerous consequences of negative refraction, the most promising in terms of applications is the ability for a slab of negative index material to produce an image from any point source. Indeed, in the extent of an equivalent homogeneous negative index material, the Snell's law simply applies using the negative index.

$$n_1 \sin i_1 = n_2 \sin i_2 \tag{4.8}$$

Here, n_1 and n_2 are the indexes and i_1 and i_2 the incident and refracted angles. The negative value of i_2 accounts for both refracted and incident beams being on the same side with respect to the normal plane. Let us consider a sound source that emits waves in a usual positive medium in front of a slab of another material. As depicted on Fig. 4.33a, geometric ray tracing predicts that, if both materials are positive, every beam from the source will cross the two interfaces between the two materials and diverge as well on the output side of the slab. By contrast, if the slab is made of a negative index material then, any diverging beam will converge in the thickness of the slab. In the latter case, provided that the slab is sufficiently thick, the beam will focus twice (Fig. 4.32b).

This way a simple parallel slab of negative material performs by itself the focusing of an image as a lens would do. It is worthy to note that the principle of such a lens does not rely on the effect of shaping the material but rather on the intrinsic properties of negative index materials. The properties of these lenses are completely different from their usual counterparts. First, a simple geometrical analysis shows that the link between the respective positions of the image and source points is:

$$i = d\frac{\tan i_2}{\tan i_1} - s = d\frac{-n_1/n_2 \cos i_1}{\sqrt{1-(n_1/n_2)^2 \sin^2 i_1}} - s, \tag{4.9}$$

where d is the slab thickness, s the distance from the point source to the input side and i the distance from the output side to the image. The consequence of this relation is that rays with different angles of incidence focus at different distances from the output side. This is a drawback since producing an image from a point source requires that all the angular components of the incident signal are focused

to a same point, which is called stigmatism. Here this requirement is fulfilled only if:

$$n_2 = -n_1, \tag{4.10}$$

which is the condition for All Angles Negative Refraction (AANR). This first condition is a strong yet possible condition for imaging with a negative metamaterial slab. In that case (4.9) reduces to:

$$i = d - s. \tag{4.11}$$

4.5.2 *Origin of the Rayleigh Resolution Limit: Toward Super Resolution*

This condition being satisfied, one can hope to build a lens whose resolution at a wavelength λ is at best $\Delta = \lambda/2$. This limitation, known as Rayleigh resolution limit, holds even in the case of no-loss materials and with a lens of infinite aperture. As pointed out by Pendry [31], its origin lies in the loss of the near field, evanescent, components from the source. If we consider the field emitted by a point source one must consider components with real wave-vectors (propagating waves) and pure imaginary wave-vectors due to the finite extension of the source. The former components are evanescent waves whose decay occurs over the distance of a few wavelengths. In the following we describe by means of a Green's function formalism [32] how the loss of these components leads to the Rayleigh resolution limit.

Let assume an infinite slab of thickness d made of a homogeneous double negative material immersed in a positive medium. Despite Green's functions are well suited to describe the response of any medium (possibly inhomogeneous) to a point source stimulus, for the sake of simplicity, both media are treated as homogeneous fluids. This assumption will be discussed further on a practical case. However, this description is still suitable to show how to enhance the resolution thanks to the integration of evanescent components. The notations and geometry used in the following parts are depicted on Fig. 4.34, where ρ_1, ρ_2,c_1 and c_2 are the densities and the sound waves velocities (phase velocities) of media 1 and 2 respectively.

The Green's function $G(\vec{x},\vec{x}')$ describes the field generated at $\vec{x}$ by a Dirac source located at $\vec{x}'$. Due to the axial symmetry of the problem and the aim to introduce the concept of wave-vectors we shall write this function as a two-dimensional spatial Fourier transform in the plane parallel to the fluid/slab interface:

$$G(\vec{x},\vec{x}') = \int \frac{\mathrm{d}^2\vec{k}_{//}}{(2\pi)^2} \mathrm{e}^{\mathrm{i}\vec{k}_{//}\left(\vec{x}_{//}-\vec{x}'_{//}\right)} g(\vec{k}_{//}, x_3, x'_3), \tag{4.12}$$

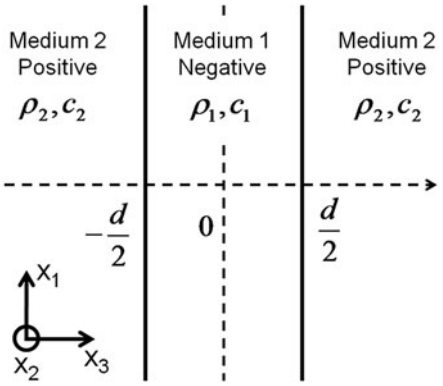

Fig. 4.34 Notations used in the Green's function analysis of the Rayleigh resolution limit and super-resolution phenomena

where $\vec{k}_{//}$ and $\vec{x}_{//}$ are the components of the wavevector and position vector parallel to the (x_1, x_2) plane. This is the function of a composite medium composed of the flat lens (medium 1) of thickness d (with faces centered on $-d/2$ and $d/2$) immersed between two semi-infinite media 2. Following the notions developed in Chap. 3 about composition of Green's functions, this Fourier Transform can be expressed by:

$$g(\vec{k}_{//}, x_3, x_3') = \frac{2\rho_1 c_1^2 \alpha_1 e^{-\alpha_2(x_3 - x_3' - d)}}{\left(\rho_1 c_1^2 \alpha_1 + \rho_2 c_2^2 \alpha_2\right)^2 e^{\alpha_1 d} - \left(\rho_1 c_1^2 \alpha_1 - \rho_2 c_2^2 \alpha_2\right)^2 e^{-\alpha_1 d}} \quad \text{for} \quad x_3' < -d/2 \quad \text{and} \quad x_3 > d/2 \tag{4.13}$$

Here, $\alpha_i = -ik_{3,(i)}$, is the component of the wave-vector perpendicular to the interface between medium 1 and medium 2.[1] This wave-vector is the key parameter since its value will account for the propagating or evanescent nature of the waves and its sign depends on the positive or negative index of the material. The component $k_{3,(i)}$ of the wave-vector is fully determined at a given frequency and $k_{//}$ by the dispersion relation of a homogeneous fluid:

$$\left(\frac{\omega}{c_i}\right)^2 = k_{//}^2 + k_{3,(i)}^2 \tag{4.14}$$

In addition, the conservation of the parallel component of the wave-vector implies that $k_{//}$ is the same in both media. One can see that (4.14) admits real solutions for $k_{3,(i)}$ (i.e., propagating waves) only if $\omega \leq k_{//} c_i$. But we have to consider the opposite case when $\omega > k_{//} c_i$ and $k_{3,(i)}$ is pure imaginary (i.e., evanescent waves). Finally, in the case of a double negative material, the wave-vector is

[1] One can note that the zeros of the denominator in (4.13) correspond to all propagating and bound modes of the system.

Table 4.2 Normal to the slab component of the wave vector is defined depending on the evanescent or propagating nature of the wave and of the sign of the medium index

	Medium 1 Negative index	Medium 2 Positive index
Propagating $\omega \geq k_{//}c_i$	$k_{3,(1)} = -\sqrt{\frac{\omega^2}{c_1^2} - k_{//}^2}$	$k_{3,(2)} = \sqrt{\frac{\omega^2}{c_2^2} - k_{//}^2}$
Evanescent $\omega < k_{//}c_i$	$k_{3,(1)} = i\sqrt{k_{//}^2 - \frac{\omega^2}{c_1^2}}$	$k_{3,(2)} = i\sqrt{k_{//}^2 - \frac{\omega^2}{c_2^2}}$

anti-parallel to direction of propagation which is accounted for by the minus sign for the real $k_{3,(1)}$. This choice of a negative sign in the case of propagating waves ensures causality as pointed out by Veselago [32]. These considerations about the wave-vectors are summarized in Table 4.2.

As shown above, in order to achieve sound focusing by means of a negative index slab, the All Angles Negative Refraction condition has to be satisfied. Since the index is defined by $n_i = 1/c_i$, it implies that $c_1 = c_2 = c$. We will further simplify the model with some loss of generality by assuming that $\rho_1 = -\rho_2 = -\rho \leq 0$. The negative sign of the density is due to the fact that medium 1 is a double negative material which means that both bulk modulus and density are negative. Therefore, the Fourier transform of the Green's function from (4.13) reduces to:

$$g(k_{//}, x_3, x'_3) = \frac{\mathrm{e}^{-\alpha(x_3 - x'_3 - 2d)}}{2\rho c^2 \alpha} \quad \text{for} \quad x'_3 < -d/2 \quad \text{and} \quad x'_3 > d/2 \tag{4.15}$$

This function has to be summed over the parallel components range $k_{//}$ of the source. This range will determine the resolution of the image. Indeed, if we assume that both propagating and evanescent modes contribute to the formation of the image (i.e., the integral is carried out for $k_{//}$ from zero to infinity[2]) then:

$$G(\vec{x}, \vec{x}') = \int_0^\infty \frac{\mathrm{d}^2 \vec{k}_{//}}{(2\pi)^2} \mathrm{e}^{\mathrm{i}\vec{k}_{//}\left(\vec{x}_{//} - \vec{x}'_{//}\right)} g\left(k_{//}, x_3, x'_3\right) = \frac{\mathrm{e}^{\mathrm{i}(\omega/c)|\vec{x} - \vec{x}_i|}}{4\pi\rho c^2 |\vec{x} - \vec{x}_i|}, \quad \text{where}$$
$$\vec{x}_i = \left(0, 0, \frac{d}{2} + d - s\right). \tag{4.16}$$

This expression is that of a spherical wave originating at the point $\vec{x}_i$. The spatial extent of this image is zero and therefore represents the perfectly reconstructed image of the point source. Comparing this results to the notations of Fig. 4.33b, we retrieve the relationship $i = d - s$. On the opposite, if we consider the usual far field situation, evanescent waves do not contribute to the image reconstruction and at a given frequency ω, the upper limit for $k_{//}$ is ω/c. Then, the Green's function

[2] The formulae: $\sqrt{\frac{\pi}{2}} \frac{\mathrm{e}^{-\alpha|\xi|}}{\alpha} = \frac{1}{\sqrt{2\pi}} \int_{-\infty}^{\infty} \frac{\mathrm{e}^{\mathrm{i}\xi x}}{\alpha^2 + x^2} \mathrm{d}x$ is used to calculate the Green's function.

describes an image similar to (4.9) convoluted by a Gaussian profile whose half-width is:

$$\Delta = 2\pi c/\omega = \lambda/2 \tag{4.17}$$

This latter case accounts for the Rayleigh resolution limit. Beating this resolution limit requires to achieve reconstruction of the image with at least a part of the evanescent spectrum from the source. Furthermore, we see that the actual resolution of an image is defined by the upper bound of the integral in (4.16). If any mechanism enables the integration of components with wave vectors up to $k_{//m} > \omega/c$, then the resolution is:

$$\Delta = 2\pi/k_m < \lambda/2, \tag{4.18}$$

which demonstrates that the system achieves super resolution.

4.5.3 Design of a Phononic Crystal Super Resolution Lens

Sub wavelength resolution imaging has been a topic of considerable interest over the past decade. As seen above, this effect requires negative refraction and the ability of a system to transmit the entire spatial Fourier spectrum from a source, including evanescent components. Here, we discuss the possibility to implement such an acoustic super-lens and go into details about the recent experimental and theoretical demonstration by Sukhovich et al. [11] using a structure consisting of a triangular lattice of steel cylinders in methanol, all surrounded by water (Fig. 4.35a).

First, negative refraction can arise from one of two mechanisms. Double negative metamaterials consist of systems including locally resonant structures which exhibit a negative effective mass and negative bulk modulus [33, 34]. Other suitable systems are phononic crystals, consisting of a periodic array of inclusions in a physically dissimilar matrix [5, 6, 9, 11, 35, 36]. Negative refraction in phononic crystals relies on Bragg scattering that induces bands with a negative group velocity. It should be noticed that, since both metamaterials and phononic crystals have complex dispersion curve, the approximation of a homogeneous media is unlikely to be satisfied over the whole frequency range. However, it is possible to design these systems such that in a narrow frequency band, they can be considered as double negative materials with an effective negative index. In order to achieve AANR, one has to design the phononic crystal such that at a given frequency, the equifrequency contour is similar to an isotropic media, i.e., is a circle. In addition, at this frequency, in order to satisfy condition $c_1 = c_2 = c$, this circle must have the same diameter as the equifrequency contour of the media that surrounds the phononic crystals lens. This requirement explains the choice of methanol as the fluid medium surrounding the steel rods in the phononic crystal so that, at a

frequency in the second band, the size of the circular equifrequency contours of the crystal could be tuned to match the equifrequency contours of water outside the crystal (Fig. 4.36). Thus, one of the important conditions for good focusing could be achieved with this combination of materials. Indeed, any liquid with a sound velocity that is small enough relative to water would have sufficed, with methanol being a convenient choice not only because it is a low-loss fluid with a low velocity (approximately two thirds the velocity in water) but also because it is readily available. In this case, in the vicinity of the frequency of 544 kHz (the operation frequency), the methanol-steel lens behaves as a negative index medium whose index is opposite to the index of water, thus achieving the AANR condition.

The second requirement to obtain sub wavelength imaging is to keep the contribution of the source evanescent modes. Following Sukhovich et al. [11], sub wavelength imaging of acoustic waves has also been shown to be possible using a square lattice of inclusions on which a surface modulation is introduced [38], a steel slab with a periodic array of slits [39], and an acoustic hyperlens made from brass fins [40]. In these demonstrations, the mechanism by which this phenomenon occurs has been attributed to amplification of evanescent modes through bound surface or slab modes of the system. In these systems, bound acoustic modes whose frequency falls is the vicinity of the operation frequency exist. In that case, provided that the lens is located in the close field of the source, some energy radiated by the evanescent modes will couple in a resonant manner to these bounded modes. The whole phononic crystal slab is excited and reemits the evanescent components necessary to the perfect image reconstruction. It is worthy to note that the amplification mechanism does not violate the conservation of energy since evanescent waves does not carry energy as pointed out by Pendry [31]. In this case, couplings with bounded modes play the role of the amplification mechanism. These modes can be studied by means of a Finite Difference Time Domain (FDTD) (see Chap. 10) simulation as shown on Fig. 4.37. If we look at the dispersion graph in the direction parallel to the water/lens interface (i.e., in the ΓK direction of the phononic crystal first Brillouin zone), we see a number of branches that corresponds to waves whose displacement is confined in the phononic crystal or at the surface of the slab. More specifically, at the operation frequency of 544 kHz, some nearly horizontal branches extend outside the water dispersion cone. These modes are likely to couple with wave vectors outside the cone at this frequency in accordance with the scheme described by Luo et al. [41].

4.5.4 Experimental and Theoretical Demonstration

Experiments have been carried out by Sukhovich [11] on a 2D phononic crystal made of 1.02-mm-diameter stainless steel rods arranged in a triangular lattice with lattice parameter of $a = 1.27$ mm. The surface of the crystal was covered by a very thin (0.01 mm) plastic film and the crystal was filled with methanol. A rectangular lens was constructed from 6 layers of rods, with 60 rods per layer, stacked in the

ΓM direction of the Brillouin zone, i.e., with the base of the triangular cell parallel to the surface. The experiments were conducted in a water tank. The ultrasound source was a narrow subwavelength piezoelectric strip, oriented with its long axis parallel to the steel rods; it was therefore an excellent approximation to a 2D point source. The spatiotemporal distribution of the acoustic field on the output side of the lens was detected with a miniature 0.40-mm-diameter hydrophone mounted on a motorized stage, which allowed the field to be scanned in a rectangular grid pattern. This setup ensures that the widths of the source and detector are smaller than the wavelength in water ($\lambda = 2.81$ mm) at the frequency of operation (530 kHz). The pressure field, shown on Fig. 4.38, exhibits a focal spot on the axis of the lens at a distance of approximately 3 mm from the output side. The resolution of this image is defined as the half-width of the pressure peak corresponding to the image. This value is determined by locating the maximum amplitude and fitting a vertical cut of the pressure field through this point by a sinus cardinal function ($\mathrm{sinc}(2\pi x/\Delta)$). The half width $\Delta/2$ is taken to be the distance from the central peak to the first minimum. The resolution at 530 kHz was found to be 0.37λ, where $\lambda = 2.81$ mm. This value is significantly less than the value of 0.5λ that corresponds to the Rayleigh diffraction limit, demonstrating that the phononic crystal flat lens achieves super-resolution.

These experimental results are supported by FDTD simulations. The FDTD method is based on a discrete formulation of the equations of propagation of elastic waves in the time and space domains on a square grid. The method is described in further details in Chap. 10. Here the whole methanol/steel phononic crystal is meshed as well as a part of the surrounding water. The limits of the simulation cell are treated under the Mur absorbing boundary condition that prevents reflections. The simulated phononic crystal slab has only 31 rods per layer in order that calculations remain compatible with computational resources. However tests have shown low influence of the reduced length. The acoustic source is simulated by a line source (0.55 mm wide) of mesh points emitting a sinusoidal displacement at frequency $v = 530$ kHz in accordance with the best experimental result. Their displacement has components parallel and perpendicular to the surface of the lens. The contour map on Fig. 4.38b shows the field of the time-averaged absolute value of the pressure. It can be seen in that an image exists on the right side of the crystal accompanied by lobes of high pressure that decay rapidly with distance from the surface of the crystal. The similarity between the experimental scheme and the FDTD mesh enables direct comparison of both experimental and simulated pressure fields. The FDTD results confirm the observation of super resolution with an image resolution of 0.35λ in excellent agreement with experiments. Both experimental and FDTD field patterns of Figs. 4.35b and 4.38 exhibit intense excitation inside the lens which is consistent with the role that bound modes are expected to play in the resonant transmission of the acoustic spectra. Theses modes, near the operating frequency, are bulk modes of the finite slab, not surface modes that decay rapidly inside the slab.

As seen above, the Rayleigh resolution limit originates from the upper limit of the Fourier spectrum transmitted to the image point which is at best ω/c in the far field regime of an imaging device. Here, since re-emitted evanescent waves can

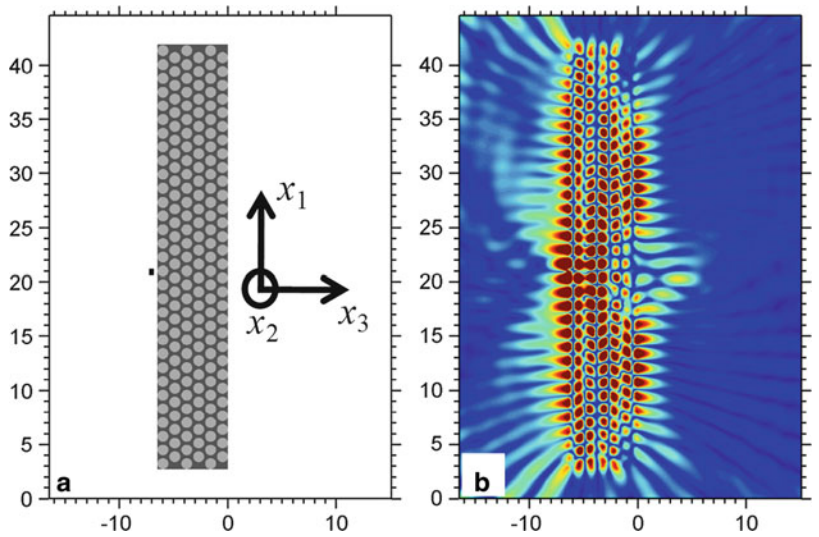

Fig. 4.35 Scheme of the system studied by Sukhovich et al. [11]. The radius of the steel inclusions is $r = 0.51$ mm with a lattice parameter of $a = 1.27$ mm. (**a**) FDTD grid used for the numerical study. The black line in front of the input side represents the source. (**b**) Averaged pressure field obtained through FTDT simulation. Note the image on the output side whose resolution (0.35λ) is below the Rayleigh limit

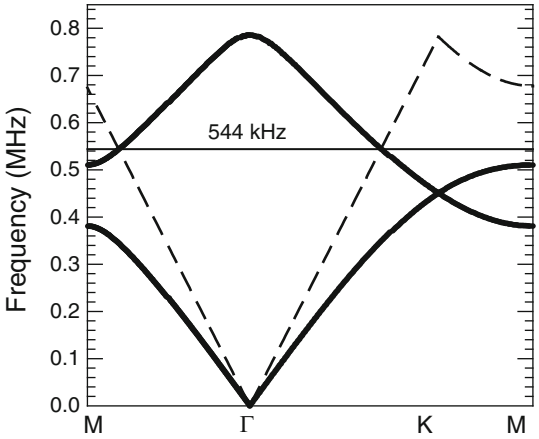

Fig. 4.36 Band structure of the methanol-steel phononic crystal after [37]. The *solid lines* represent the dispersion curves. The dispersion relation of the surrounding medium (water) is drawn as *dashed lines*. The second band exhibits a negative group velocity and intersects the water cone on a circular equifrequency at 544 kHz

contribute to the image, the resolution beats this criterion. By this mechanism one can virtually build an image up to an arbitrary resolution provided all evanescent modes are amplified and a sufficient time is available to reach the steady state regime for all evanescent modes. However, despite the absence of losses in the

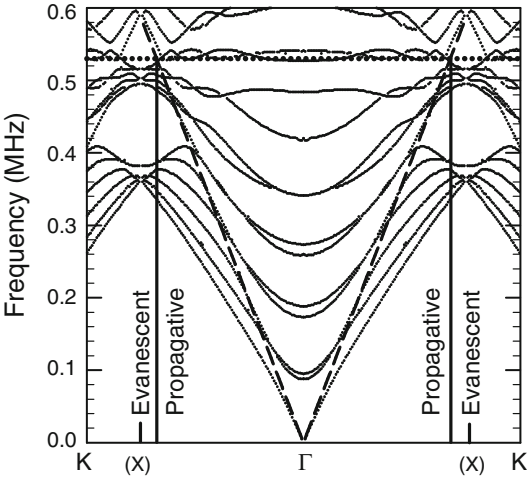

Fig. 4.37 Band structure diagram of the whole phononic crystal slab and water system in the direction parallel to the lens surface (FDTD calculation after [37]). Each curve corresponds to an acoustic mode propagating either in the phononic crystal slab or at the water/slab interface. The operation frequency (544 kHz) is indicated as a *horizontal dotted line*. The *straight dashed lines* are the dispersion relation of water. The *x*-axis range has been extended to the fist Brillouin zone ΓK of the triangular lattice

simulation scheme, the simulated resolution value is only 0.35λ. This fact indicates that the transmission of evanescent waves does not occur over the full Fourier spectra but rather up to a limiting cut-off value k_{m}. The previous analysis of super resolution in term of Green's function assumed the constituent material of the lens to be a homogeneous negative index material and did not discuss the possible origins of limitations to the transmitted Fourier spectra of the source. In the practical case when a phononic crystal, which is an inhomogeneous periodic material, is used as the lens, only modes with wave vector k parallel to the lens surface that is compatible with the periodicity of the phononic crystal in that same direction can couple to the sound source. In other words, all evanescent modes cannot contribute to the reconstruction of the image. The upper bound of the integration is determined by the largest wave vector k_{m} parallel to the lens surface that is compatible with the periodicity of the phononic crystal in that same direction and that can be excited by the sound source. In Fig. 4.37, the dispersion curves of the slab immersed in water are shown in the direction parallel to the lens surface. The dashed diagonal lines are the dispersion curves of acoustic waves in water and the dotted horizontal line represents the operating frequency. At this frequency, the wave vector components of the incident wave with $k_{//} < \omega/c$ can propagate in the crystal; they will form an image according to classical geometric acoustics. Components with $k_{//} > \omega/c$ will couple to the bound modes of the slab provided that these bound modes dispersion curves are in the vicinity of the operating frequency. In this way, the existence of many modes of the slab with nearly flat dispersion curves in the vicinity of the operating frequency is beneficial for achieving super resolution, as mentioned in [37]. One might imagine that

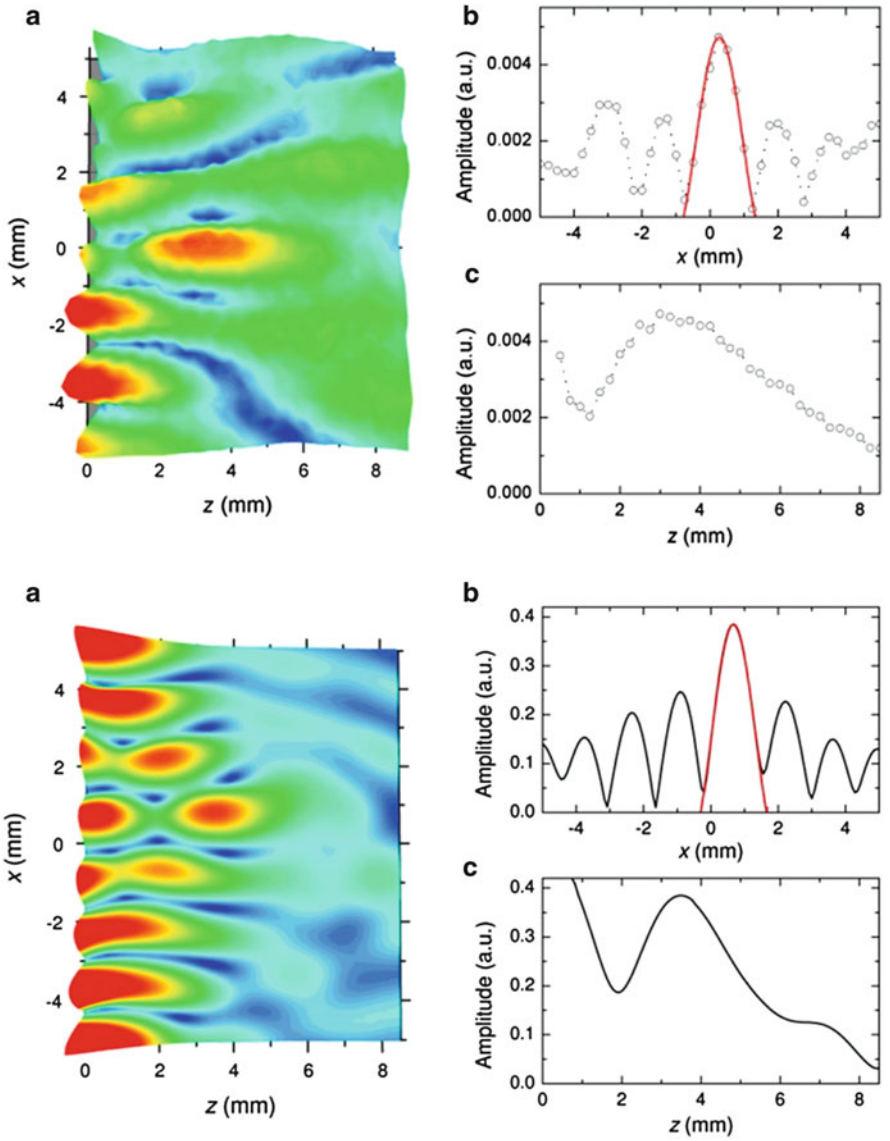

Fig. 4.38 Comparison of experimental (*top*) and FDTD simulation (*bottom*) results after Sukhovich et al. [11] showing the averaged pressure filed and pressure profiles along the lens axis and the output side

evanescent waves with transverse wave vector of any magnitude above ω/c could couple with bound modes. However, the modes that propagate through the thickness of the lens must resemble those of the infinite periodic phononic crystal. The symmetry of the waves inside the lens must therefore comply with the triangular symmetry of the phononic crystal. More precisely, the modes of the crystal are periodic in k-space with a period equal to the width of the first 2D triangular

Brillouin zone. This is the reason why the x-axis of Fig. 4.37 has been extended up to the K point of the hexagonal lattice reciprocal space. If an incident wave has a wave vector above the first Brillouin zone boundary, then it will couple to a mode having a wave vector that can be written as $\vec{k}'_{//} = \vec{k}_{//} + \vec{G}$ where $\vec{G}$ is a reciprocal lattice vector and $\vec{k}$ lies in the first Brillouin zone. In our case, since the first Brillouin zone of a triangular lattice extends from $-4\pi/3a$ to $4\pi/3a$ in the ΓK direction (parallel to the lens surface), the information carried by incident evanescent waves with transverse wave vector components,

$$k_{//} < k_{\mathrm{m}} = 4\pi/3a, \tag{4.19}$$

will contribute to the formation of the image. According to (4.11), with this definition, one finds that the best possible image resolution is:

$$\frac{\Delta}{2} = \frac{3a}{4}, \tag{4.20}$$

Applying this estimate to our phononic crystal with $a = 1.27$ mm, and a wavelength in water at 530 kHz of 2.81 mm, the minimum feature size that would be resolvable with this system is 0.34λ. This estimate matches results very well for the best resolution found for this system (0.34λ) presented in Sect. 4.2, and with experiment (0.37λ).

4.5.5 *Effects of Physical and Operational Parameters on Super Resolution*

In this section, we explore the effects of several factors on the image resolution of the phononic crystal flat lens. These factors include operational parameters such as the source frequency and the position of the source and geometrical factors such as the width and thickness of the lens. By exploring modifications to the system, we aim to shed light on the parameters that have the greatest impact on the imaging capabilities of the phononic crystal lens and understand their effects as they deviate from the best operating conditions.

4.5.5.1 Operating Frequency

Up to now, the operating frequency of the source was chosen to be 530 kHz, as in [6], this value was chosen as a compromise between proximity with bounded modes required for evanescent waves coupling and the AANR frequency in order to achieve the best experimental resolution. We now focus on the effects of the operating frequency in the 510 to 560 kHz range by means of numerical simulations and experimental measurements. Figure 4.39a shows the image resolution and

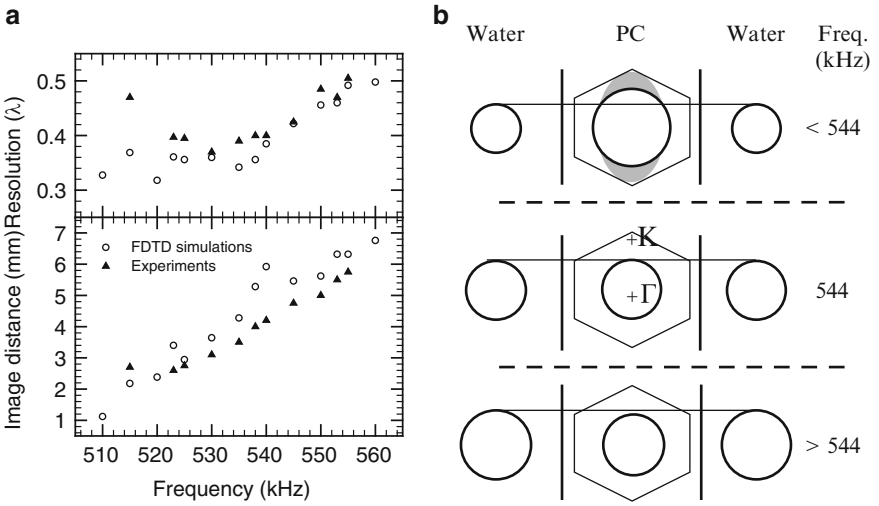

Fig. 4.39 Effects of the operating frequency after [37]. (**a**) Resolution and distance of the image as a function of the operating frequency. Results from experiments (*triangles*) are compared to FDTD simulation (*circles*). (**b**) Schematic representation of the transmission through the phononic crystal lens based on the equifrequency contours shapes. The equifrequency contour of the phononic crystal lens is represented as a *circle* inside the first Brillouin zone of the hexagonal infinite crystal. The gray areas illustrate the existence of bound modes with frequency very close to the operating frequency

distance of the focus from the exit surface of the lens as a function of the operating frequency. Experiments and calculations are in reasonable agreement from 523 to 560 kHz. Experiments exhibit an optimum resolution (0.37λ) at 530 kHz as discussed above. As expected, experimental values are higher than the computed values since practical imperfections in the lens fabrication and measurement noise lower the resolution of the focus. However, the difference does not exceed 0.05λ which is excellent. For increasing frequencies, the image lateral width increases up to the Rayleigh value (0.5λ) while the focus forms farther from the lens output side. These trends are confirmed in both experiments and FDTD results. However, no clear minimum of the resolution is observed in the simulations.

The observation of an optimum resolution has been interpreted in terms of a trade off between the AANR condition and the excitation of bound modes of the phononic crystal [37]. Figure 4.39b depicts the EFC in water and in the phononic crystal for different frequencies as circles of different diameters. The occurrence of super-resolution is discussed with respect to the operating frequency of 544 kHz which is the frequency of AANR expected from simulations.

First, if the source frequency is tuned *lower than 544 kHz*, super resolution is achieved with a resolution below 0.39λ. Since the operating frequency is lower than 544 kHz, the equifrequency contour of water is a smaller circle than the EFC inside the crystal. All components of the incident wave vectors corresponding to propagating modes can be negatively refracted by the crystal, i.e., the AANR

condition is satisfied. However, the mismatch of the equifrequency contours diameters leads to a negative effective index of refraction with magnitude greater than one, causing the different components from the source to focus at different places. On another hand, operating frequencies well below 544 kHz are close to the flat bands of bound modes in the phononic crystal slab, allowing for efficient excitation by the evanescent waves from the source (Fig. 4.37). These modes are depicted as a gray region on the EFC of the slab in Fig. 4.39b. Thus, the gain from the amplification of evanescent modes is retained and super-resolution is achieved.

At the frequency of 544 kHz the EFC of water and the phononic crystal have the same diameter resulting in an effective index of -1. This condition implies a perfect focusing of all propagating components of the source into a single focal point. However Fig. 4.37 shows that the flat bands of bound modes of the lens are now well below the operating frequency, which means that coupling with these modes and amplification of the evanescent waves during transmission is now inefficient. The experimental optimum of the lateral resolution at 530 kHz occurs between the bound mode frequencies (510 kHz) and the perfect matching of the equifrequency contours (544 kHz).

In the case of *frequencies above 544 kHz*, the EFC of water has now a greater diameter than the EFC of the phononic crystal and the AANR condition is not matched. A part of the propagating components experience total reflection at the water/lens interface and the resolution worsens up to 0.5λ at 555 kHz.

These results confirm the importance of the design of the phononic crystal superlens with respect to two conditions. First, one has to meet the AANR condition, which requires that the phononic crystal be a negative refraction medium with a circular EFC matching the EFC of the outside medium (water). Second, bound modes must exist in the phononic crystal whose frequencies are close to the operating frequency so that amplification of evanescent components may occur. The optimum frequency is found as the best compromise between those two parameters.

Finally, the effect of the operating frequency on the image distance can be understood according to acoustic ray tracing. Here, since the magnitude of the effective acoustic index of the phononic crystal decreases as the frequency increases, the image appears farther from the lens exit surface for higher frequencies [see (4.9)]. This trend, confirmed by experiments as well as simulations (see Fig. 4.39a) shows the high sensitivity of the image location to changes in frequency. Here, tuning the frequency from 523 to 555 kHz shifts the image from 2.6 to 5.75 mm. A change over 6 % in the frequency is able to tune the focal spot distance over 220 %.

4.5.5.2 Distance from the Source to the Lens

Here, we consider the effects of the position of the source with respect to the phononic crystal surface. Super resolution requires coupling of the evanescent waves from the source to bound modes in the phononic crystal in order to achieve

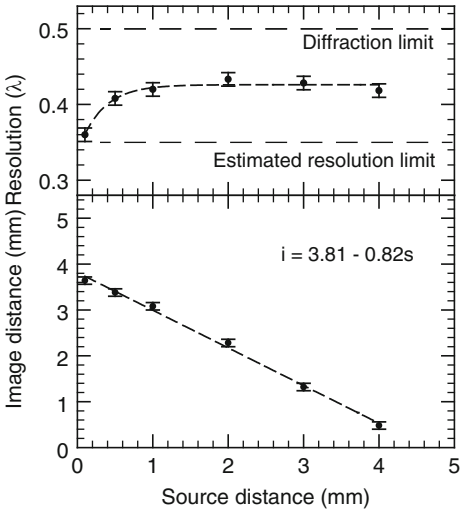

Fig. 4.40 Plot of the resolution and image distance as a function of the source distance

amplification and re-emission. This process is thus only possible if the phononic crystal lies in the near field of the point source at a distance where evanescent components are not too much attenuated. In terms of sizes, this means that distance from source to lens and the period of the phononic crystal (lattice constant) are comparable in magnitude. A question arises whether or not the detailed heterogeneous structure of the phononic crystal can be ignored and replaced by a continuous model of a negative index material. This question was addressed from a numerical point of view by varying the distance between the point source and the surface at the optimum frequency of 530 kHz. The measured effects are the position of the source with respect to the exit face and the lateral resolution of the focus as shown on Fig. 4.40. Indeed, if the phononic crystal can be modeled by a homogeneous negative index material slab, geometrical ray tracing implies that the distance from lens to focus is described by (4.11). The dashed horizontal lines represent the Rayleigh diffraction limit (0.5λ) and the estimated maximum resolution limit (0.34λ) calculated in Sect. 4.5. It results that as the distance between the source and the face of the lens is increased, excitation of the bound modes is less and less effective and the resolution decreases. For this range of image distances, the resolution remains smaller than the Rayleigh diffraction limit. The fact that this limit is not reached on the plot is related to the close distances which range from 0.036λ to 1.4λ. The lens is always in the near field of the source for the studied range. One expects that for larger distances the resolution will reach the Rayleigh diffraction limit, accompanied by loss of super-resolution. It should be noted that the source cannot be placed farther than one lens thickness from the lens itself in order to get a real image. Thus, to observe the complete loss of super-resolution would require to significantly increase the lens thickness as well as the source distance which is demanding for a computational point of view.

The Green's function model described in Sect. 4.5.2 shows that if all evanescent and propagating modes are contributing the image is perfectly reconstructed as a point source at a distance $d-s$ from the exit face of the lens. This position is in accordance with geometric rays tracing in two media with opposite refraction indices. It could be shown that if the two media had some low acoustic index mismatch or if the lens media had uniaxial anisotropy in normal incidence axis direction [32], the relation would still be linear. This linear behavior is indeed observed thanks to simulation data on Fig. 4.40 where the focus location fits a linear relation with a slope of -0.82 with respect to source location. However, the intercept of this curve is not exactly the thickness of the lens ($d = 6.52$ mm), as expected from (4.11). We have seen that the operating frequency could change dramatically the focus location since it defines the effective index of the phononic crystal. Here the results are presented at the frequency of 530 kHz which is not the exact value of the AANR condition when an index of $n = -1$ is achieved. The value for 530 kHz is rather $n = -1.07$. Acoustic ray tracing predicts that if n is the effective index of the phononic crystal relative to water, then the focus position for a source placed very close to the lens is $d/|n|$. This would predict an intercept at 6.09 mm, still far from the observed value. Thus, the frequency effect over index alone is insufficient to explain completely the discrepancy. This discrepancy is therefore most probably due to the fact that the assumption of a homogeneous negative medium is poorly valid in the case of a phononic crystal because of the similar length scales between the lattice parameter, lens thickness, wavelength and the source distance. At least, it is less valid than in the case of metamaterial slabs [42] where the resonant inclusions have sizes well below the wavelength.

4.5.5.3 Geometry of the Phononic Crystal Lens

The geometry of the lens itself has been studied in terms of its effects on resolution and the location of the image. The respective effects of the thickness and width of the phononic crystal lens are discussed successively. The width of the lens has been studied from the experimental and computational point of views. The picture of a semi infinite slab (in the x_1 and x_2) directions used for the Green's function model is quite different in the context of simulations and experiments where the width of the lens is measured along x_1 by the number of rod inclusions in each layer parallel to the surface. The question raised by the limited width of the lens is similar to what is called aperture in the context of optics. The spatially limited transmission due to the finite extent of a lens is responsible for a loss of resolution due to the convolution of any image by an Airy function. Thus, a sufficient width has to be chosen so that this limitation is low enough in order to demonstrate the super resolution effect. Sukhovich et al. [5] have used lenses of 15, 31 and 61 rods per layer in crystals made of 6 layers, all other parameters being constant. The behavior of the lenses with 31 and 61 rods per layer are similar and suitable to exhibit super resolution. The position of the image and resolution as a function of the position of the source

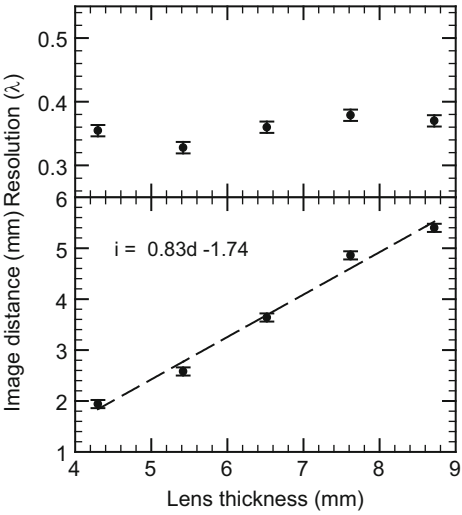

Fig. 4.41 Effects of the number of layers. Lateral resolution and distance of the image as a function of the number of layers

(Fig. 4.41) were almost identical. By contrast, the results for the narrower 15 rods per layer are significantly different. This effect was attributed to the small aspect ratio (2.5) of this lens inducing significant distortions. For lenses wider than 31 rods, the aspect ratio is greater than 5 and does not affect the results.

For what concerns the thickness of the lens, it can be varied by changing the number of layers of inclusions. Robillard et al. [37] simulated thicknesses of 4, 5, 6, 7 and 8 layers for the case with a width of 31 rods per layer. The distance from the source to the surface was maintained at 0.1 mm and the corresponding results are shown in Fig. 4.41. It follows that, within the range of measurement error, the resolution does not change with width as expected. This fact is also confirmed by the authors by the existence of similar bound modes in the vicinity of the operating frequency whatever the lens thickness. The frequencies of the bound modes that are responsible for super-resolution do not vary significantly as the thickness changes. Last point, always according to the ray tracing and Green's models, the distance of the image is expected to be linearly dependent on the lens thickness. This fact is observed as well but the fitted value of this slope is not one, as expected in the case of a homogeneous negative medium, but 0.83. As discussed earlier in this paragraph, the lens made of an effective homogeneous medium may not be a valid hypothesis in these conditions. Again, the discrepancy between the slope of 0.83 compared to one indicates the thickness mismatch between effective homogeneous slabs and phononic crystal slabs [42].

4.5.5.4 Location of the Source in the Direction Parallel to the Lens

The position of the source in a direction parallel to the slab input face plays a role that is linked to the amplification mechanism of evanescent components from the source. Necessary couplings with bound modes of the phononic crystal slab and near field proximity implies that this mechanism is sensitive the heterogeneous structure of the phononic crystal. Especially, efficient coupling requires that displacement fields of the bound modes and evanescent waves overlap in space. Since the lens excitation exhibits high pressure lobes in front of each steel cylinder when super resolution is achieved, it is assumed that the bound modes involved have similar displacement patterns. Thus, by shifting the source in a direction parallel to the slab the efficiency of the couplings is expected to change and result in modification of the super resolution effect. This process was simulated by a source facing the gap midway between two cylinders of the phononic crystal. In this case, the resolution falls to 0.54λ as can be seen by the wider focus on Fig. 4.42a, b.

Experiments confirm these results are in accordance with experimental results; moving the source parallel to the surface from the position opposite a cylinder (best resolution) by only a quarter of its diameter caused the image resolution to degrade from 0.37λ to 0.47λ.

Thus, looking at Fig. 4.42a gives an understanding of the bound modes displacement. The pressure exhibits lobes of maximum amplitude between cylinders and consequently the displacement amplitude would show maxima in front of each cylinder and nodes between them. Placing the source at any of the nodes of the displacement field prevents evanescent waves from coupling efficiently with the bound modes.

4.5.5.5 Disorder

The properties of Phononic Crystals rely on the coherent summation of the Bragg scattered components of acoustic waves on the successive planes of the crystal. Because of this coherent character, any deviation from perfect order inside the crystal structure is expected to introduce diffusion effects that are detrimental to imaging properties. Especially, the super-resolution effect that is described in this section should be sensitive to such defects. This hypothesis has been verified from both the experimental and numerical point of view [11]. Figure. 4.42c, d show FDTD results that assume some random deviation in the rods position from the perfect triangular lattice configuration. This positional disorder in the numerical model has a standard deviation of 5 %, which corresponds to an upper limit for the experimental crystal. The experimental measurements were found to be very sensitive to disorder in the position of the steel rods. These results confirm in that disorder in the phononic crystal is detrimental to the quality of the image and for some random realizations can even eliminate the focusing property of the lens.

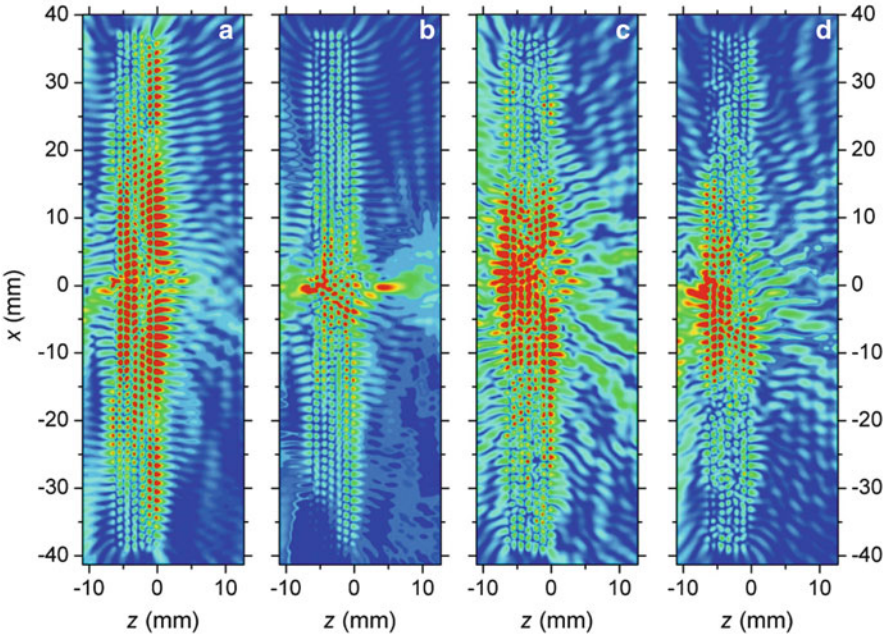

Fig. 4.42 Influence of the location of the source in the direction parallel to the lens and of the disorder after [11]. The contour maps of the normalized average absolute value of pressure calculated via FDTD at a frequency of 530 kHz for the phononic crystal lens imaging are plotted. (**a**) The line source is located at 0.1 mm from the left lens surface and centered with respect to a surface cylinder at $x = 0$. (**b**) Same simulation as (**a**) but with the source shifted down by $a/2$ in the direction parallel to the surface of the lens. (**c**) and (**d**) show two lenses with positional disorder of the steel rods showing imperfect focusing (**c**) and loss of focusing (**d**)

4.6 Band Structure Design and Impact on Refraction

As shown before, 2D and 3D phononic crystals have been extensively studied and implemented for their frequency dependent (ω-space) effects on sound or elastic wave propagation. Especially, absolute band gaps have led to a variety of guiding, confinement and filtering designs. The astonishing demonstration of sound tunneling is also related to the presence of band gaps. On the other hand, negative bands and the subsequent negative refraction that occurs at the interface of some phononic crystals and the surrounding media is a property related to the shape of the EquiFrequency Contour (EFC) of the dispersion curves in the wave-vectors plane (k-space). For the purpose of achieving super resolution imaging with a phononic crystal lens, one has to design a phononic crystal with circular EFCs. These two effects, band gaps and all-angle negative refraction, have received much attention from the community since the first reports on sonic crystals. However, as expected from the behavior of elastic waves in genuine crystals, a wider variety of properties should result from the periodic arrangement of phononic crystals constituents. The propagation of waves is always fully understandable by means of the dispersion relations, i.e. the ω and k-spaces. Since dispersion curves are determined by

geometrical (sizes, symmetry) and material (stiffness, density) parameters, phononic crystals can be designed in order to exhibit advanced spectral (ω) and directional (k) properties based on the analysis of the dispersion relations. In this section we show how the design, especially the symmetry, of a phononic crystal, can lead to strongly anisotropic effects such as positive, negative and even zero angle refraction at a single frequency. Other effects such as collimation, beam splitting and phase controlling are also predicted. Eventually, we discuss the opportunity to control the respective phases between different acoustic beams (φ-space) and its possible implementation on acoustic logic gates.

4.6.1 Square Equifrequency Contours in a PVC/Air Phononic Crystal

In 2009, Bucay et al. [43] have described theoretically and computationally the properties of a phononic crystal made of polyvinylchloride (PVC) cylinders arranged as a square lattice embedded in a host air matrix. We will develop this section of Chap. 4 from the properties of this representative system. This PVC/air system exhibits an absolute band gap in the 4–10 kHz range followed by a band exhibiting negative refraction. The band structure for the infinite periodic phononic crystal is generated by the Plane Wave Expansion (PWE) method and plotted in Fig. 4.43b. In the 13.5 kHz equifrequency plane, the second negative band defines a contour of nearly square shape centered on the M point of the first Brillouin zone. This shape appears clearly in Fig. 4.43c which shows a contour map of the dispersion surface taken between frequency values 13.0 and 16.0 kHz extended to several Brillouin zones. Though the properties of such an arrangement can be reproduced in other systems of suitable symmetry and material parameters, we describe here the parameters used in that particular demonstration. The spacing between the cylinders (lattice parameter) is $a = 27$ mm and the radius of the inclusions is $r = 12.9$ mm. The PVC/Air system parameters are: $\rho_{\mathrm{PVC}} = 1364$ kg/m^3, $c_{\mathrm{t,PVC}} = 1000$ m/s, $c_{\mathrm{l,PVC}} = 2230$ m/s, $\rho_{\mathrm{Air}} = 1.3$ kg/m^3, $c_{\mathrm{t,Air}} = 0$ m/s, and $c_{\mathrm{l,Air}} = 340$ m/s (ρ is density, c_{t} is transverse speed of sound, and c_{l} is longitudinal speed of sound). The PVC cylinders are considered as infinitely rigid and of infinite height. This assumption of rigidity simplifies the band structure calculation and is justified by a large contrast in density and speed of sound between the solid inclusions and the matrix medium. Again, the results gathered from this analysis are applicable to other solid/air phononic crystals of the same filling fraction because, in reference to other solids, air has extremely small characteristic acoustic impedance.

Bucay et al. [43] have focused on the consequences on acoustic propagation in the passing bands with such square shaped EFCs. Here we summarize these effects and their possible applications in acoustic imaging and information processing. The next paragraphs use the schematic of Fig. 4.43a on which a PVC/air phononic crystal slab is surrounded by air. This schematic corresponds to the FDTD simulation space. One

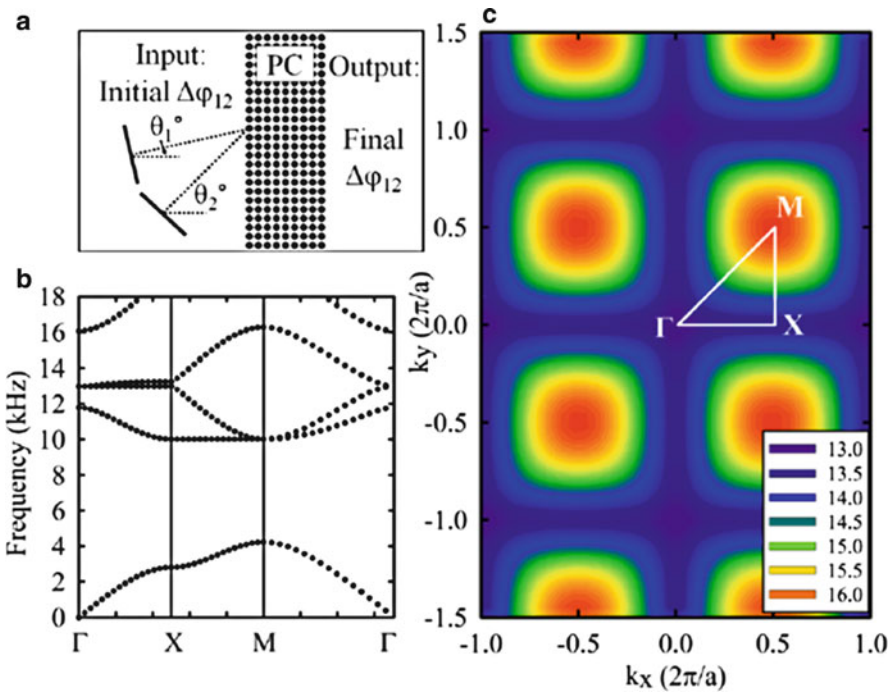

Fig. 4.43 Schematic and band structure of the PVC/air system after Bucay et al. [183]. (**a**) Schematic illustration of the FDTD simulation cell. The acoustic sources can assume any incident angle to the phononic crystal face and be set with any relative phase difference. (**b**) Band structure generated by PWE method along the edges of the first Brillouin zone (pictured in (**c**)). (**c**) EFCs (extended zone scheme of irreducible Brillouin zone) in range of 13.0–16.0 kHz

or several beams impinge on the input side. Each source on the input side of the simulation space is modeled by a slanted line of grid points consistent with the desired incidence angle of the source. The nodes along this line are displaced in a direction orthogonal to the source line as a harmonic function of time. These sources can assume any incident angle to the phononic crystal face and can be ascribed any relative phase difference, thus allowing for complete analysis of the phononic crystal wave vector space (k-space) and phase-space (φ-space). The output side is reserved for the detection of exiting acoustic signals.

4.6.2 Positive, Zero, and Negative Angle Refraction, Self-Collimation

First, looking at the EFC contour at a given frequency of 13.5 kHz, it appears that the square symmetry of the phononic lattice has a strong impact on the band structure (Fig. 4.44). Indeed, while at very low frequencies the dispersion relations are linear (low frequency parts of the acoustic branches), the higher order branches

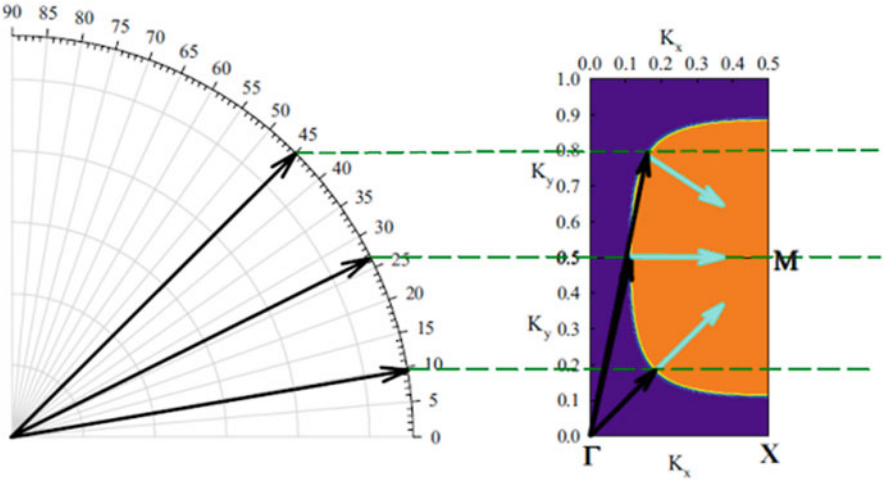

Fig. 4.44 Determination of the refraction angles of several incident beams from the EFC of the PVC/air system

considered at the frequency of 13.5 kHz have direction dependent properties. These *k*-dependent properties appear themselves in the almost square shape of the equifrequency contour. The equivalent media formed by the PVC/air has to be considered as anisotropic. This particular EFC is plotted in Fig. 4.44 along with the EFC in air at the same frequency. The EFC of the PVC/air system has been extended over another Brillouin zone in the K_y direction on this plot in order to exhibit one complete face of the square which is centered on the M point. Since the surrounding medium is linear and isotropic in the operating frequency range its EFC is simply circular. Let us now discuss the different cases of the beam refraction induced by the unusual shape of the EFCs.

In order to clearly describe these cases, we remind the reader how the wave vector and group velocity of a refracted beam is determined from the angle of an incident beam.

The conservation of frequency and parallel to surface ($k_{//}$) component of wave vector is required. These rules are written in Eqs.4.21 and 4.22 where the subscripts i and r stand for *incident* and *refracted*.

$$\omega_{\mathrm{i}} = \omega_{\mathrm{r}}, \tag{4.21}$$

$$\overrightarrow{k_{//\mathrm{i}}} = \overrightarrow{k_{//\mathrm{r}}} + \overrightarrow{G}, \tag{4.22}$$

The presence of a vector $\overrightarrow{G}$ of the reciprocal lattice will be discussed later, in the non-periodic media it is a zero vector. In other words, the normal component of the wave vector $k_{\perp}$ is determined such that the wave vector $k_{\mathrm{r}} = k_{\perp \mathrm{r}} + k_{//\mathrm{r}}$ in the second medium matches a dispersion curve at the frequency ω_{i}. If such a matching

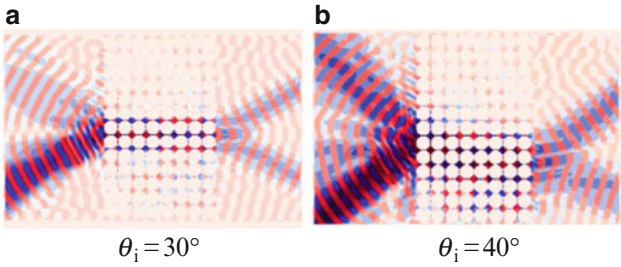

Fig. 4.45 Zero refraction and negative refraction occur at the same frequency, in the same PVC/air system depending only on the incidence angle. The incident beams are oriented upward at angles of (**a**) 30° and (**b**) 40° respectively

point exists, a refracted beam exists, otherwise the incident beam undergoes total reflection. The couple (k_r ,ω_r) defines a point of the Brillouin zone at which the group velocity can be determined by (4.7). It must be noted that, contrary to the case of an isotropic media, the wave vector and group velocity might not be collinear in the general case. This can be seen in Fig. 4.44 where the wave vectors are depicted by black arrows and the group velocity vectors by blue arrows.

From these rules and Fig. 4.44 it follows that any beam that impinges on the phononic crystal with an incidence angles lower that 5° cannot couple to any propagation mode of the phononic crystal and thus will be completely reflected. This can be seen as a directional band gap. Between 5° and 55° waves are refracted and propagate in the phononic crystal and several cases are distinguished. Below 28°, refracted waves have a group velocity vector (blue arrows) with a positive parallel (K_y) component. They undergo classical positive refraction. At the singular angle of 28°, the contour is flat in the K_y direction such that the group velocity will be perfectly oriented toward the x axis. Such behavior corresponds to a zero angle of refraction and is quite unusual. An illustration of this phenomenon is shown in Fig. 4.45a with a FDTD result of the averaged pressure field. An incident beam at 30° is oriented toward the surface of a PVC/air crystal slab. Since the incidence angle is very close to the predicted zero refraction angle (28°) it is refracted and the beam follows a path close to the x axis.

In Fig. 4.45b, a beam with higher incidence angle is negatively refracted, in accordance with the previous discussion. The ability of this system to achieve positive, negative and zero angle refraction at a single frequency has been successfully tested experimentally and theoretically by Bucay et al. [43]. One should note that the vicinity of the 28° incidence angle coincides with small degrees of refraction. One could define an incidence range that gives rise to refracted angles reasonably close to zero. As an example, for incidence angle between 20° and 30° the angle of refraction is within in the −2° to 2° range. Thus, from this point of view this system is able to combine a wide angle input wave into a nearly collimated beam. This ability called *self-collimation* is pretty unusual and could have significant uses in the field of acoustic imaging. The discussed system can also enable the

propagation in the same volume of the phononic crystal of two non-collinear incident beams. This spatial overlapping of two waves carrying non-identical signals offers interferences conditions that might be useful for information processing as we shall see later.

4.6.3 Beam Splitting

Another striking property of such a system is the presence of two output beams as seen on Fig. 4.45. The incident beam impinges from the bottom part of the simulation cell. The upper beam on the input side is a partial reflection. On the exit side, the beam splits into balanced parts. This phenomenon, confirmed experimentally [43], is striking since Snell's law of refraction does not account for such behavior. Optical analogues of such an effect are birefringent crystals which discriminate light into several beams with respect to its polarization or beam splitters that share incident energy into two output beams. Again, this analogy does not account for the radically different origins of this effect in optics and acoustic phononic crystals. Indeed, while optic beam splitters take advantage of balanced transmission and reflection coefficients by means of suitable surface coatings, the phononic crystal beam splitter produces two identical refracted beams, that both have propagated through the phononic crystal following the same path. In the latter case, the splitting effect relies only on the properties of wave coupling between periodic (phononic crystal) and homogeneous (air) media. Potential applications of this spontaneous beam splitting effects are discussed in the following sections. Here we describe its origins.

The schemes in Fig. 4.46 show the equifrequency planes in a system composed of a phononic crystal slab similar to the PVC/Air system immersed in a fluid medium (air). The plot extends over two Brillouin zones. The operating frequency is 13.5 kHz, which corresponds to a square EFC of the phononic crystal. Note that the circular EFC in air is larger than the first Brillouin zone of the phononic crystal. Let us now apply coupling rules for an incident wave to propagate inside the phononic crystal. In (4.22) we have introduced an additional vector $\vec{G}$ that belongs to the reciprocal lattice. Indeed, in crystalline structures as in any periodic structure the momentum conservation can be satisfied modulo a certain vector $\vec{G}$. This conservation rule for sonic waves is analogous to the one governing phonon diffusion in solids [44]. The processes which involve a zero G vector are called natural processes. They ensure complete conservation of the crystal momentum, while non-zero G vector processes (Umklapp) ensure momentum conservation due to the contribution of the crystal total momentum. The latter involve a wave vector outside of the first Brillouin zone. From this rule follows that for a given incidence angle, the incident beam can couple to several modes inside the phononic crystal. The wave vectors of these modes lie in distinct Brillouin zones. Since the extent of the EFC in air is twice as large as the Brillouin zone, two of $k_{//}$ are possible for the propagation into the phononic crystal. On the output side these two different modes

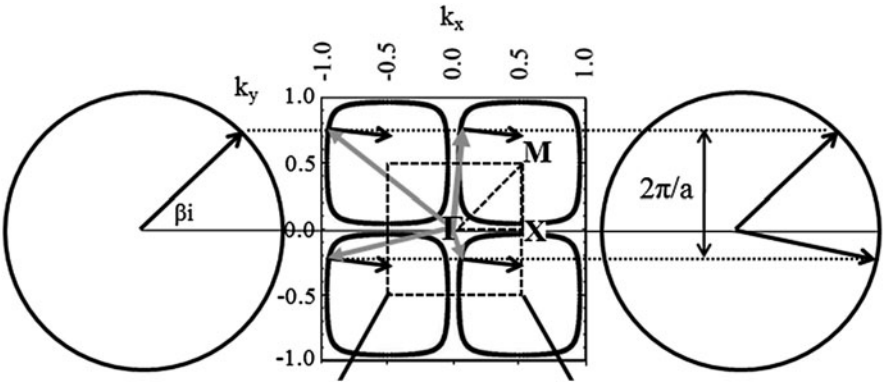

Fig. 4.46 Determination of the refraction angles of several incident beams from the EFC of the PVC/air system. The central scheme depicts an extended zone EFC contour of the phononic crystal. *Gray arrows* are wavevectors while *black arrows* are the group velocity vector

couple back to the surrounding media according to the same rules, which account for the presence of two beams.

The remarkable property of the multiple modes inside the phononic crystal is that they have similar group velocity vectors (black arrows) but different wavevectors (gray arrows). It results that they will only split on the output side but share the exact same path inside the crystal.

Additionally, Fig. 4.46 shows that, on the opposite side of the zero incidence line, another beam might couple with exactly the same set of wave vectors inside the crystal. Then, two beams can produce exactly the same effects and are called complementary. Complementary waves will have incidence angles $\theta_0 + \Delta\theta$ and $-\theta_0 + \Delta\theta$ with θ_0 being the zero-refraction angle.

4.6.4 Phase Control

Except for the case of complementary incident waves, any couple of incident beams will be refracted at different refraction angles and thus accumulate a certain phase difference while propagating through the crystal. One should remark that, here again, refracted waves in the phononic crystal have somewhat uncommon properties since their group velocity is nearly parallel to the normal to the crystal/air interface (Fig. 4.46) while their *k*-vector, has a wide range of possible orientations due to the incidence angle. Group velocity and wave vector being non-collinear simply means that energy and phase propagates in different directions. In the vicinity of the zero angle refraction, a wide span of Bloch waves exists with group velocities that coincide with small degrees of refraction, allowing refraction to occur between propagating waves within the nearly same volume of crystal. This is shown through the high slope around 0° in Fig. 4.47a which represents the angle of incidence of the

input beam as a function of the angle of refraction in the bulk of the phononic crystal slab.

A fine analysis of the square EFC shows that, while the group velocity of different refracted beams have nearly the same zero angle of refraction, their wave vectors quite different. Since group velocity describes the propagation of the energy while the wave vector k is related to the propagation of phase, this fact shows that beams propagating in close directions in the phononic crystal might accumulate significantly different phase shifts.

To investigate this effect, Swinteck and Bringuier [45–47] have calculated the phase shift accumulated per unit length of a phononic crystal slab as a function of the incidence angle. Two impinging waves with wave vectors $\overrightarrow{k_1}$ (angle θ_1) and $\overrightarrow{k_2}$ (angle θ_2) excite several Bloch modes throughout the k-space of the phononic crystal. As seen in the *beam-splitting* effect, because the extent of the first Brillouin zone is smaller than the circular EFC in the surrounding media, each incident wave will couple to two Bloch modes that correspond to complementary waves. These two Bloch modes are noted $\overrightarrow{k_{1A}}$ and $\overrightarrow{k_{1B}}$ in Fig. 4.48a and are necessary to describe the wave physics in this phononic crystal in terms of phase. Each of these wave vector pairs has a unique refraction angle noted as α_1 and α_2. The following calculations will focus on the phase shift accumulated between Bloch modes $\overrightarrow{k_{1A}}$ and $\overrightarrow{k_{2A}}$ only (noted $\varphi_{1A,2A}$), though similar discussion would lead to compatible results for the second pair of modes. These two Bloch wave vectors are expressed as:

$$\overrightarrow{k_{1A}} = \frac{2\pi}{a}\left\{k_{1x}\vec{i} + k_{1y}\vec{j}\right\} \tag{4.23}$$

$$\overrightarrow{k_{2A}} = \frac{2\pi}{a}\left\{k_{2x}\vec{i} + k_{2y}\vec{j}\right\} \tag{4.24}$$

where k_{1x} and k_{1y} are the components of the wave vector $\overrightarrow{k_{1A}}$ and k_{2x} and k_{2y} are the components of the wave vector $\overrightarrow{k_{2A}}$ (in units of $2\pi/a$). $\vec{i}$ and $\vec{j}$ are unit vectors along axes x and y respectively.

Each incident beam $\vec{k}$ is refracted by an angle α and travels in the phononic crystal along a path that is simply:

$$\vec{r} = L\vec{i} + L\tan(\alpha)\vec{j} \tag{4.25}$$

where L is the slab thickness. The phase accumulated at the exit face of the slab with respect to the input point is:

$$\varphi = \vec{k}\cdot\vec{r} = \frac{2\pi L}{a}\left\{k_x + \tan(\alpha)k_y\right\} \tag{4.26}$$

It follows that the phase difference between Bloch modes with wave vectors $\overrightarrow{k_{1A}}$ and $\overrightarrow{k_{2A}}$ can be expressed as:

$$\varphi_{1A,2A} = \overrightarrow{k_{1A}} \cdot \overrightarrow{r_1} - \overrightarrow{k_{2A}} \cdot \overrightarrow{r_2} = \frac{2\pi L}{a}\left\{k_{1x} + \tan(\alpha_1)k_{1y} - k_{2x} - \tan(\alpha_2)k_{2y}\right\} \quad (4.27)$$

Let us formulate a few remarks about this result. First, to evaluate this phase shift it is useful to plot it as a function of the incidence angle θ_1 of one input beam the other beam being a constant reference beam. The angle (28.1°) for which zero while angle refraction occurs is a preferred choice. Second, as expected, the result depends linearly on the thickness of the slab. Third, computing this phase shift can be done by extracting the components, (k_{1x}, k_{1y}) and (k_{2x}, k_{2y}), used in (4.27) from the EFC data in Fig. 4.45. Finally, the calculated phase shift per unit length is plotted in Fig. 4.47b along with FDTD results that agree very well with the above analysis. Looking closely at (4.27), one understands that the phase shift has two origins. First, the travel paths inside the phononic crystal for the both waves are different ($\overrightarrow{r_1} \neq \overrightarrow{r_2}$). The second effect comes from the difference in phase velocities ($\left|\overrightarrow{k_{1A}}\right| \neq \left|\overrightarrow{k_{2A}}\right|$). Waves of different phase velocities traveling different paths certainly will develop a phase shift. From Fig. 4.47b one can deduce the phase difference between a pair of beams which is of crucial importance since it determines how exiting beams interfere. It is worth noting that the steel/methanol system described in Sect. 4.5 exhibits, at the considered operating frequencies, circular EFCs centered on the Γ point. In such a configuration phase and group velocity are collinear and anti-parallel. Such a system wouldn't produce substantial phase shifts between two Bloch modes that are nearly collinear.

Figure 4.48b shows that outgoing beams intersect each other on the output side in two points. These points are places where the relative phase between two beams can be found by measure of the interference state. The choice of the two incidence angles higher and lower than 28.1 (the zero angle of refraction) is important. Indeed it ensures that one beam is refracted positively and the other one negatively, while forming the intersection points on the exit side. In the end, the incidence angles of the two beams determine wave vectors $\overrightarrow{k_1}$ and $\overrightarrow{k_2}$ and the angles of refraction α_1 and α_2 which give the phase shift. Therefore incidence angle selection is proposed as a leverage to modulate the relative phase between propagating acoustic beams.

4.6.5 Implementation of Acoustic Logic Gates

More recently, it has been proposed to use these interference effects to implement an acoustic equivalent of the so-called Boolean logic gates [47] on the basis of phase control by means of a phononic crystal slab. Here we discuss the example of the NAND gate which is identified as universal since the implementation of any other Boolean logic gate is feasible by associating several NAND gates [48]. The NAND gate is a two inputs function which truth table is described in Fig. 4.49a. The setup of Bringuier et al. [47] relies on a phononic crystal slab and two permanent sources S1

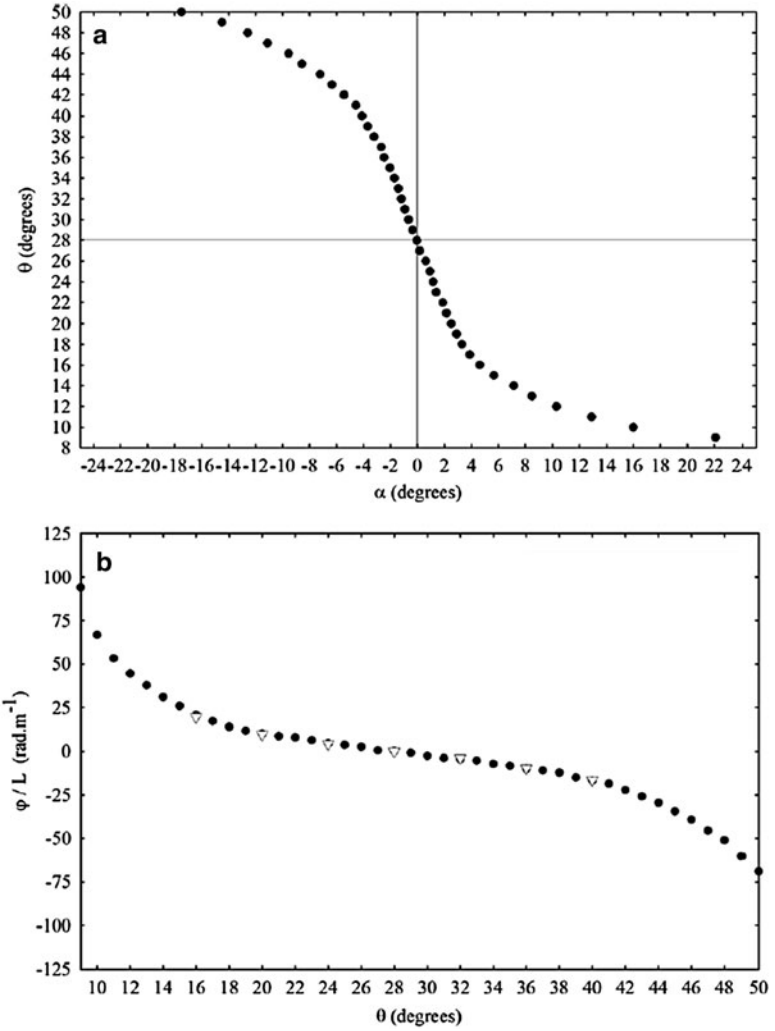

Fig. 4.47 (**a**) Angle of the incident beam as a function of its refraction angle. The graph can be read as follows: one obtains a 0° refracted beam inside the phononic crystal when the incidence angle is 28°. (**b**) Phase shift per unit length of phononic crystal as a function of the incidence angle. The phase shift is evaluated with respect to a zero refracted beam (*Circles*: analytical solution. *Triangles*: results from FDTD calculation)

and S2 impinging at the same point of the input face. The angles of incidence are such that these beams are not complementary waves, i.e., their paths do not perfectly overlap in the phononic crystal slab. The following demonstration is based on FDTD simulations on the PVC/air system described above. In this scheme it is straightforward to keep a given phase relation between the two permanent sources S1 and S2. In this particular case, they they impinge in-phase on the input side of the phononic

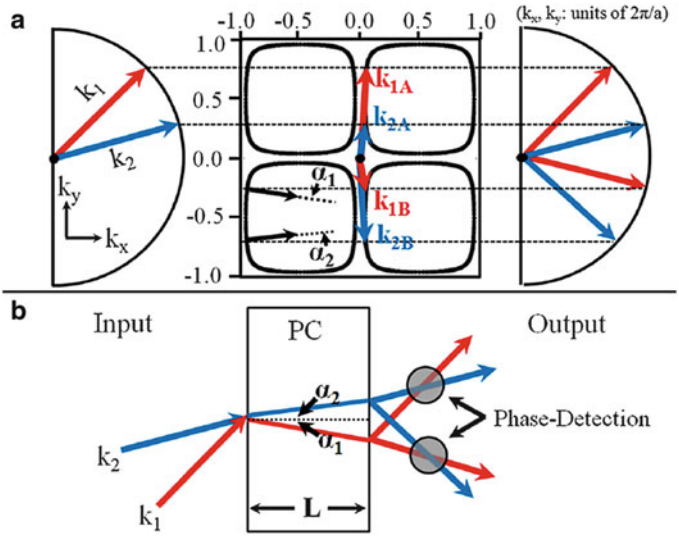

Fig. 4.48 (**a**) (*k*-space) Bloch modes excited in the PVC/air system by two waves having different angles of incidence. (**b**) (real space) paths of the corresponding waves in the phononic crystal slab. After Swinteck et al. [46]

crystal. Because their incidence angles are 10° and 38°, the two sources will refract negatively and positively in accordance with the Fig. 4.48b. The phase shift on the output side is calculated thanks to (4.27) and is evaluated to be 2π radians. This results in constructive interference on the output side between the centers of the exiting beams. At this particular point where the interferences are constructive, a detector D is positioned. This "detector" simply indicates that the averaged pressure is recorded over a given cut which makes an angle 24° (i.e., in between 10° and 38°). The corresponding pressure profile is presented on the left side of Fig. 4.49b. The position of the constructive interference point is indicated by a vertical dashed line which, indeed, corresponds to a maximum of the pressure. This state describes the zero inputs state of the NAND gates. In this regime the continuous high level of pressure is interpreted as a 1 output from the gate.

The authors model the inputs of the NAND by two additional beams I1 and I2 which are the corresponding complementary waves (19° and 50°) to the sources, S1and S2, respectively. As compared to the permanent sources, I1 and I2 are set such that their phases are π radians on the input side. It results from this condition that whenever I1 is turned on, it perfectly overlaps the path of S1 in the phononic crystal (because these are complementary waves) and since their phase difference is π, they interfere destructively. It results that only S2 contributes to the averaged pressure at the detector point as shown on Fig. 4.49c. The same analysis holds if I1 is off and I2 is on. The last case corresponds to having both inputs emitting waves simultaneously. In this case S1 and I1 as well as S2 and I2 interfere destructively

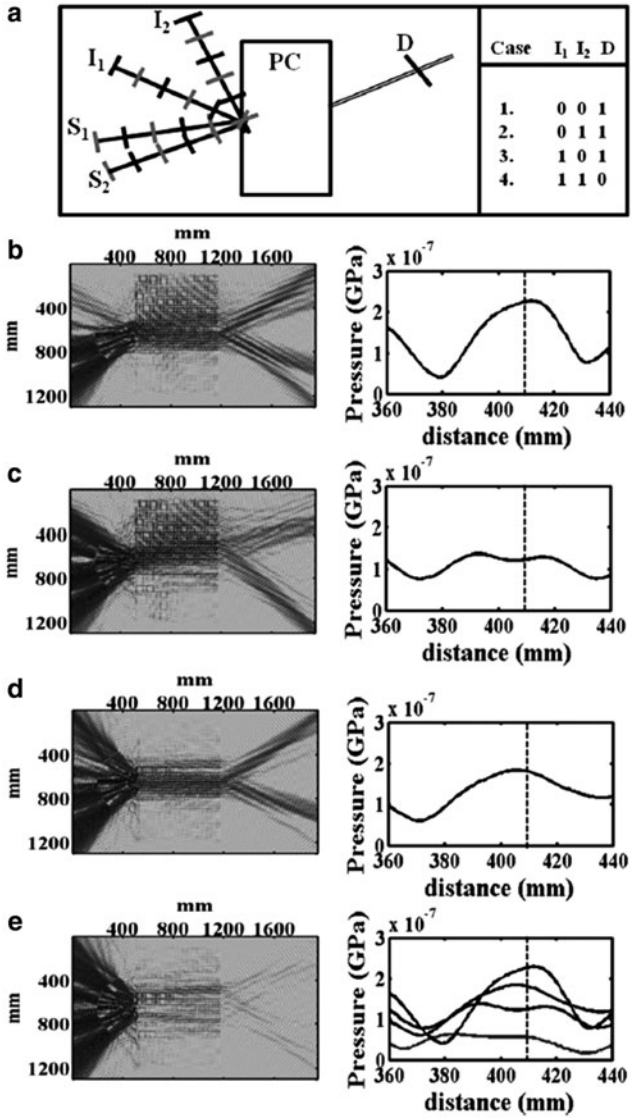

Fig. 4.49 Implementation of the NAND gate with phononic crystals. The system consists of a phononic crystal with the same square EFC characteristics as in the PVC/Air system and two permanent sources S_1 and S_2 are incident at different angles

and this case exhibits the minimal pressure at the detector point among all other cases.

The situation when "I1 is emitting" (or "I1 is not emitting") means that the first input of the NAND gate is at state 1 (or state 0). By establishing a threshold value just above the minimal pressure, the output is defined to be in state 1 if the pressure

is above the threshold and in state 0 if the pressure is below the threshold. Finally, the only configuration that produces a 0 output state is the state with I_1 and I_2 both emitting waves. This complies with the truth table of the NAND gate. This study demonstrates another possible application of the full dispersion properties (frequency, wave vector and phase) of phononic crystals in the field of information processing.

4.7 Conclusion

In this chapter, we have focused on 2D and 3D phononic crystals and their unusual properties. After having introduced the necessary concepts of Bravais lattices and their corresponding Brillouin zones, we have summarized how phononic crystals properties can be investigated experimentally especially in the ultrasonic frequency range. The discussion then focused on spectral aspects of phononic crystals. The existence of band gaps is the first property of phononic crystals investigated theoretically and experimentally. Because of the evanescent character of waves whose frequency falls into the band gaps, tunneling of sound has been demonstrated. However, band gaps despite the wealth of applications they bring (sound isolation, wave guiding, resonators, filtering...) are not the only striking phenomena in phononic crystals. Other phenomena observed in the passing bands have been studied in details such as negative refraction. Negative refraction occurs when the wave vector and the group velocity are anti-parallel in a material. The similarities between negative refraction and the negative index metamaterials have been discussed. This chapter also provides a wealth of details about experimental conditions of negative refraction. Later sections have focused on the conditions required to use negative refraction in combination with close field coupling to a phononic crystal slab in order to achieve super-resolution, i.e., imaging a source point with a better than half-wavelength resolution. Finally, we have briefly described recent developments about the impact of the phononic crystal symmetry on refraction properties. A model system exhibiting anisotropic propagation properties has been described by its refraction properties as a function of their incidence angles. This type of system has been demonstrated in the context of self-collimation, beam-splitting, phase controlling and a possible implementation of logic gates.

Throughout the chapter it has been shown that, despite the variety of possible implementations of phononic crystals, their properties can always be described in the frame of Bragg reflections of the acoustic or elastic waves that interfere constructively or destructively. The consequences of periodicity manifest themselves in the dispersion relations that *fully* describe the spectral, directional and phase properties of propagation in phononic structures. From this point of view the analogy between phononic crystals and natural crystalline material is complete. It follows that, the complete spectrum of opportunities offered by periodic artificial structures is extremely large and still not fully explored.

References

1. Z. Liu, X. Zhang, Y. Mao, Y.Y. Zhu, Z. Yang, C.T. Chan, P. Sheng, Locally resonant sonic materials. Science **289**, 1734 (2000)
2. P. Sheng, X. Zhang, Z. Liu, C.T. Chan, Locally resonant sonic materials. Physica B **338**, 201 (2003)
3. J.H. Page, S. Yang, M.L. Cowan, Z. Liu, C.T. Chan, P. Sheng, 3D phononic crystals, in *Wave Scattering in Complex Media: From Theory to Applications*, (Kluwer Academic Publishers: NATO Science Series, Amsterdam, 2003) pp. 283–307
4. A. Sukhovich, J.H. Page, B. van Tiggelen, Z. Liu. Resonant tunneling of ultrasound in three-dimensional phononic crystals. *Physics in Canada* **60**(4), 245 (2004)
5. A. Sukhovich, L. Jing, J.H. Page, Negative refraction and focusing of ultrasound in two-dimensional phononic crystals. Phys. Rev. B **77**, 014301 (2008)
6. S. Yang, J.H. Page, Z. Liu, M.L. Cowan, C.T. Chan, P. Sheng, Ultrasound tunnelling through 3D phononic crystals. Phys. Rev. Lett. **88**, 104301 (2002)
7. S. Yang, J.H. Page, Z. Liu, M.L. Cowan, C.T. Chan, P. Sheng, Focusing of sound in a 3D phononic crystal. Phys. Rev. Lett. **93**, 024301 (2004)
8. F. Van Der Biest, A. Sukhovich, A. Tourin, J.H. Page, B.A. van Tiggelen, Z. Liu, M. Fink, Resonant tunneling of acoustic waves through a double barrier consisting of two phononic crystals. Europhys. Lett. **71**(1), 63–69 (2005)
9. J.H. Page, A. Sukhovich, S. Yang, M.L. Cowan, F. Van Der Biest, A. Tourin, M. Fink, Z. Liu, C.T. Chan, P. Sheng, Phononic crystals. Phys. Stat. Sol. (b) **241**(15), 3454 (2004)
10. J.H. Page, P. Sheng, H.P. Schriemer, I. Jones, X. Jing, D.A. Weitz, Group velocity in strongly scattering media. Science **271**, 634 (1996)
11. A. Sukhovich, B. Merheb, K. Muralidharan, J.O. Vasseur, Y. Pennec, P.A. Deymier, J.H. Page, Experimental and theoretical evidence for subwavelength imaging in phononic crystals. Phys. Rev. Lett. **102**, 154301 (2009)
12. Zeitschrift fur Kristallographie, vol, **220**, issues 9–10, ed. by I.E. Psarobas, pp. 757–911 (2005)
13. T.E. Hartman, Tunneling of a wave packet. J. Appl. Phys. **33**, 3427 (1962)
14. J.H. Page, S. Yang, Z. Liu, M.L. Cowan, C.T. Chan, P. Sheng, Tunneling and dispersion in 3D phononic crystals. Z. Kristallogr. **220**, 859–870 (2005)
15. M. Sigalas, M.S. Kushwaha, E.N. Economou, M. Kafesaki, I.E. Psarobas, W. Steurer, Classical vibrational modes in phononic lattices: theory and experiment. Z. Kristallogr. **220**, 765–809 (2005)
16. J. Liu, L. Ye, D.A. Weitz, P. Sheng, Phys. Rev. Lett. **65**, 2602 (1990)
17. X.D. Jing, P. Sheng, M.Y. Zhou, Phys. Rev. Lett. **66**, 1240 (1991)
18. R.S. Penciu, H. Kriegs, G. Petekidis, G. Fytas, E.N. Economou, J. Chem. Phys. **118**, 5224 (2003)
19. G. Tommaseo, G. Petekidis, W. Steffen, G. Fytas, A.B.. Schofield, N. Stefanou, J. Chem. Phys. **126**, 014707 (2007)
20. M.L. Cowan, J.H. Page, Ping Sheng, Phys. Rev. B **84**, 094305 (2011)
21. J. Li, C.T. Chan, Double-negative acoustic metamaterial. Phys. Rev. E **70**, 055602(R) (2004)
22. T. Still, W. Cheng, M. Retsch, R. Sainidou, J. Wang, U. Jonas, N. Stefanou, G. Fytas, Phys. Rev. Lett. **100**, 194301 (2008)
23. R. Sainidou, N. Stefanou, A. Modinos, Formation of absolute frequency gaps in three-dimensional solid phononic crystals. Phys. Rev. B **66**, 212301 (2002)
24. H. Zhao, Y. Liu, G. Wang, J. Wen, D. Yu, X. Han, X. Wen, Phys. Rev. B **72**, 012301 (2005)
25. V. Leroy, A. Bretagne, M. Fink, H. Willaime, P. Tabeling, A. Tourin, Appl. Phys. Lett. **95**, 171904 (2009)
26. C. Croënne, E.J.S. Lee, Hefei Hu, J.H. Page, Special Issue on Phononics, ed. by Ihab El Kady and Mahmoud I Hussein, in AIP Advances, **1**(4), (2011)
27. A.V. Akimov et al., Phys. Rev. Lett. **101**, 33902 (2008)
28. J.A. Turner, M.E. Chambers, R.L. Weaver, Acustica **84**, 628–631 (1998)

29. H. Hu, A. Strybulevych, J.H. Page, S.E. Skipetrov, B.A. van Tiggelen, Nature Phys. **4**, 945–948 (2008)
30. V.G. Veselago, The electrodynamics of substances with simultaneously negative values of ε and μ. Usp. Fiz. Nauk **92**, 517 (1964)
31. J.B. Pendry, Negative Refraction Makes a Perfect Lens. Phys. Rev. Lett. **85**, 3966 (2000)
32. P.A. Deymier, B. Merheb, J.O. Vasseur, A. Sukhovich, J.H. Page, Focusing of acoustic waves by flat lenses made from negatively refracting two-dimensional phononic crystals. Revista Mexicana De Fisica **54**, 74 (2008)
33. J. Li, K.H. Fung, Z.Y. Liu, P. Sheng, C.T. Chan, in *Physics of Negative Refraction and Negative Index Materials*, Springer Series in Materials Science, vol. 98, Chap. 8 (Springer, Berlin, 2007)
34. P. Sheng, J. Mei, Z. Liu, W. Wen, Dynamic mass density and acoustic metamaterials. Physica B **394**, 256 (2007)
35. X. Zhang, Z. Liu, Negative refraction of acoustic waves in two-dimensional phononic crystals. Appl. Phys. Lett. **85**, 341 (2004)
36. K. Imamura, S. Tamura, Negative refraction of phonons and acoustic lensing effect of a crystalline slab. Physical Review B **70**, 174308 (2004)
37. J.-F. Robillard, J. Bucay, P.A. Deymier, A. Shelke, K. Muralidharan, B. Merheb, J.O. Vasseur, A. Sukhovich, J.H. Page, Resolution limit of a phononic crystal superlens. Physical Review B **83**, 224301 (2011)
38. Z. He, X. Li, J. Mei, Z. Liu, Improving imaging resolution of a phononic crystal lens by employing acoustic surface waves. Journal of Applied Physics **106**, 026105 (2009)
39. F. Liu, F. Cai, S. Peng, R. Hao, M. Ke, Z. Liu, Parallel acoustic near-field microscope: A steel slab with a periodic array of slits. Physical Review E **80**, 026603 (2009)
40. P. Sheng, Metamaterials: Acoustic lenses to shout about. Nature Materials **8**, 928 (2009)
41. C. Luo, S.G. Johnson, J.D. Joannopoulos, J.B. Pendry, Subwavelength imaging in photonic crystals. Phys. Rev. B **68**, 045115 (2003)
42. V. Fokin, M. Ambati, C. Sun, X. Zhang, Method for retrieving effective properties of locally resonant acoustic metamaterials. Physical Review B **76**, 144302 (2007)
43. J. Bucay, E. Roussel, J.O. Vasseur, P.A. Deymier, A.-C. Hladky-Hennion, Y. Pennec, K. Muralidharan, B. Djafari-Rouhani, B. Dubus, Positive, negative, zero refraction, and beam splitting in a solid/air phononic crystal: theoretical and experimental study. Phys. Rev. B **79**, 214305 (2009)
44. G.P. Srivastava, *The Physics of Phonons*. (A. Hilger, 1990)
45. N. Swinteck, J.-F. Robillard, S. Bringuier, J. Bucay, K. Muralidharan, J.O. Vasseur, K. Runge, P.A. Deymier, Phase-controlling phononic crystal. Appl. Phys. Lett. **98**, 103508 (2011)
46. N. Swinteck, S. Bringuier, J.-F. Robillard, J.O. Vasseur, A.C. Hladky-Hennion, K. Runge, P.A. Deymier, Phase-control in two-dimensional phononic crystals. J. Appl. Phys. **110**, 074507 (2011)
47. S. Bringuier, N. Swinteck, J.O. Vasseur, J.-F. Robillard, K. Runge, K. Muralidharan, P.A. Deymier, Phase-controlling phononic crystals: Realization of acoustic Boolean logic gates. The Journal of the Acoustical Society of America **130**, 1919 (2011)
48. A.P. Godse, D.A. Godse, *Digital Logic Circuits* (Technical Publications Pune, Pune, India, 2010)
49. A.R. Selfridge, Approximate Material Properties in Isotropic Materials, *Transactions on Sonics and Ultrasonics* SU-32, 381 (1985)